

# JGR Solid Earth

## RESEARCH ARTICLE

10.1029/2024JB030538

### Key Points:

- Digital rock physics characterizes pore structures but finite-difference simulations yield higher velocities
- Modeling is done by integrating digital and theoretical rock physics to simulate wave responses and interpret multi-frequency data
- Fractured-vuggy carbonates exhibit lower velocities and greater dispersion compared to other types

### Correspondence to:

J. Ba,  
jba@hhu.edu.cn

### Citation:

Pang, M., Ba, J., Carcione, J. M., Balcewicz, M., Siebert, M., Tang, G., & Saenger, E. H. (2025). Structural and elastic properties of carbonate rocks with different pore types based on digital and theoretical rock physics. *Journal of Geophysical Research: Solid Earth*, 130, e2024JB030538. <https://doi.org/10.1029/2024JB030538>

Received 18 OCT 2024

Accepted 18 FEB 2025

### Author Contributions:

**Conceptualization:** Mengqiang Pang, Jing Ba, Erik H. Saenger  
**Data curation:** Jing Ba, Genyang Tang  
**Formal analysis:** Jing Ba, José M. Carcione, Martin Balcewicz, Mirko Siebert, Genyang Tang, Erik H. Saenger  
**Funding acquisition:** Jing Ba  
**Investigation:** Mengqiang Pang, Jing Ba, Martin Balcewicz  
**Methodology:** Mengqiang Pang, Jing Ba, José M. Carcione, Genyang Tang  
**Project administration:** Jing Ba  
**Resources:** Jing Ba  
**Software:** Mengqiang Pang, Martin Balcewicz  
**Supervision:** Jing Ba, José M. Carcione  
**Validation:** Mengqiang Pang, Jing Ba, José M. Carcione, Mirko Siebert, Genyang Tang  
**Visualization:** Mengqiang Pang, Martin Balcewicz  
**Writing – original draft:** Mengqiang Pang, Jing Ba

## Structural and Elastic Properties of Carbonate Rocks With Different Pore Types Based on Digital and Theoretical Rock Physics

Mengqiang Pang<sup>1,2</sup>, Jing Ba<sup>1</sup> , José M. Carcione<sup>1,3</sup> , Martin Balcewicz<sup>2</sup> , Mirko Siebert<sup>2</sup> , Genyang Tang<sup>4</sup> , and Erik H. Saenger<sup>2,5,6</sup> 

<sup>1</sup>School of Earth Sciences and Engineering, Hohai University, Nanjing, China, <sup>2</sup>Hochschule Bochum, Bochum, Germany,

<sup>3</sup>National Institute of Oceanography and Applied Geophysics—OGS, Trieste, Italy, <sup>4</sup>China University of Petroleum (Beijing), Beijing, China, <sup>5</sup>Fraunhofer IEG - Institution for Energy Infrastructures and Geothermal Energy, Bochum, Germany, <sup>6</sup>Institute of Geology, Mineralogy, and Geophysics, Ruhr-University Bochum, Bochum, Germany

**Abstract** Carbonates are characterized by a complex system of pores, caves, vugs and fractures that significantly influence fluid flow and the physical behaviors of rocks. Six rock samples are taken from a carbonate reservoir in China's Sichuan Basin to perform computed tomography (CT), X-ray diffraction and thin section analyses. The samples are classified into fractured, fractured-vuggy and pore-cavity types based on their microstructural properties. Ultrasonic and low frequency tests are performed with different pressures and fluids to measure the frequency dependence of the elastic properties. The relationships between the pore types and the elastic properties are investigated, showing that there is no direct correlation between velocity and porosity for these tight carbonates. Furthermore, the elastic properties of rocks with different structure types are quite different, suggesting that the pore structure dominates the elastic velocities. The CT data are used to reconstruct digital rocks to analyze the complex pore structure. We apply a finite difference (FD) method to estimate the elastic velocities. However, the FD simulations give higher values than the ultrasonic measurements. The discrepancy is due to the limited accuracy of the CT scans, which does not capture the micro-pore structures of rocks. We consider the microscopic pores and cracks and develop a reformulated rock physics model by incorporating the theories of differential equivalent medium and squirt flow based on the simulated elastic moduli. The model can effectively interpret the experimental multi-frequency data and describe the wave response of the carbonates with different pore types. This work contributes to characterize the multiscale pore structure and understand the structural and acoustic properties of carbonate rocks. It bridges multi-frequency data and provides relevant insights and methods by integrating digital and theoretical rock physics.

**Plain Language Summary** Carbonate rocks can be classified into fractured, fractured-vuggy and pore-cavity rocks based on their complex pore structures or types, and furthermore, the physical behaviors of different types can vary considerably. Laboratory measurements have shown that the relationship between elastic properties and porosity is not intuitive. Digital rock physics can effectively characterize the pore structure of rocks and contribute to the understanding and interpretation of the complex macroscopic properties. However, due to the limited quality of the scan images, it is difficult to fully capture the microscopic pores/cracks, resulting in finite difference simulations that generally differ from the experiments. We create an improved rock physics model based on the numerical simulations by taking into account the neglected part of the micro-pore structures. By combining theoretical and digital rock physics, the model can effectively interpret multi-frequency data. This study shows that pore structure characterizes the elastic wave responses of the tight carbonate rocks better than porosity.

## 1. Introduction

Carbonate reservoirs are important for meeting the global energy demands due to their rich resources and reserves (Liang et al., 2023; Phukan et al., 2024). The rock of these reservoirs has a complex pore system including multiscale fractures, caves, vugs, and pores (Bagrintseva & Chilingar, 2007; Lan et al., 2015; Malki et al., 2023), which significantly affects the seismic propagation (Carcione et al., 2010, 2012; Misaghi et al., 2010; Zhang et al., 2021, 2022; Zou et al., 2023). Theoretical and experimental studies have shown the significant differences in the petrophysical behaviors of carbonates (Aliakbardoost & Rahimpour-Bonab, 2013; Borgomano et al., 2019; Jin et al., 2017; Lubis and Harith, 2014; Mollajan & Memarian, 2016). In recent years, some studies have

**Writing – review & editing:** Jing Ba, José M. Carcione, Martin Balcewicz, Mirko Siegert, Genyang Tang, Erik H. Saenger

classified carbonate rocks into two types (Agersborg et al., 2009; She et al., 2016; Singh et al., 2021), three types (Dubiel et al., 2012; Qi et al., 2020; Rosid et al., 2017; Yue et al., 2024), or four types (Li, Mu, et al., 2020; Zhao et al., 2016) of intergranular pore, fractured, fractured-vuggy, pore-cavity-fracture, and pore-cavity types based on pore structure and type.

The complex structure of carbonate rocks poses challenges in predicting critical properties such as permeability, storage capacity, acoustic velocity and mechanical behaviors (Borgomano et al., 2017; El-Bagoury, 2024; He et al., 2020; Wu et al., 2016). Recently, advances of computed tomography (CT) have accelerated the development of digital rock physics (DRP) techniques (Andrä et al., 2013a, 2013b; Pang et al., 2024a, 2024b; Sakhaee-Pour and Bryant, 2014). This approach digitizes rock minerals, skeletons and pore spaces and enables the numerical determination of permeability, fluid flow as well as elastic and electrical responses (Garboczi & Day, 1995; Kadyrov et al., 2022; Zhu et al., 2023b). Garboczi and Day (1995) performed the static simulations using the finite element method to obtain the effective elastic properties of materials. Saenger et al. (2005) performed finite difference (FD) simulations to derive effective elastic properties, while subsequent studies, such as Sun et al. (2019) and Li, Li, et al. (2020), explored the fluid flow effects and electrical responses using advanced digital cores constructed from high-resolution CT scans. Tan et al. (2021) used CT images and FD simulations to investigate how microcracks affect the elastic properties of digital carbonate rock.

DRP is widely used to investigate structural features of rocks in the subsurface, including porosity, connectivity, and the size and radius of pore openings (Keehm, 2003; Madonna et al., 2013; Okabe & Blunt, 2004; Saxena et al., 2019). It uses multi-resolution scans and image processing on rock samples to obtain a comprehensive overview from the microscopic level to the macroscopic level, providing important information about rock structures and minerals (Saenger & Bohlen, 2004; Saenger, Lebedev, et al., 2016; Saenger, Vialle, et al., 2016; Siegert et al., 2022). Yu et al. (2019) analyzed the fracture properties of shale rock using CT scans at different pressures. Wang et al. (2022) evaluated minerals and micro-pore structures by creating digital rocks with multi-component fractures.

In particular, core-scale CT scans can combine various experimental measurements such as ultrasonic, low-frequency, porosity, permeability and electrical tests to better characterize the petrophysical and mechanical properties of rocks (Gonzalez et al., 2022). However, the resolution of core-scale CT scanning is limited by equipment capability and sample size, obscuring rock features and making accurate identification of microscopic pore structures difficult (Botha & Sheppard, 2016; Chawshin et al., 2021; Li et al., 2016). The limited image resolution often leads to discrepancies between laboratory measurements and numerical estimates (Andrä et al., 2013b; Dvorkin et al., 2011; Lissa et al., 2021). Sarout et al. (2017) compared the geometries (crack density, aspect ratio and size) of heat-treated marble samples derived from elastic moduli measured in the laboratory with those derived from 2D and 3D microscope images of the same samples (Delle Piane et al., 2015) and found significant differences in crack opening size and aspect ratio.

It has been shown that the pore system in tight reservoir rocks is very complex and contains both macro- and micropores (Bailly et al., 2019; de Vries et al., 2017; Lai & Wang, 2015; Zhu et al., 2023a), where the microscopic structure content is low but can significantly affect the physical properties of the rocks (Ba et al., 2017; Carcione et al., 2013; David & Zimmerman, 2012; Guo & Fu, 2024; Guo et al., 2022, 2024; Gurevich et al., 2009, 2010; Pang et al., 2022). Published work defines the pore space that can be covered and recognized by low-resolution (core-scale) CT scans as macropores and the pores below the resolution of the scan as micropores (Okabe & Blunt, 2007; Peng et al., 2014; Tahmasebi and Kamrava, 2018; Wu et al., 2019). Recently, the characterization of rock microstructures by using multiband/scale data and petrophysical theories has become an important topic (Ba et al., 2023; Bailly et al., 2019; Durrani et al., 2023; Mena-Negrete et al., 2022; Sarout et al., 2017; Zhang et al., 2019). We consider this approach as a solution to the problem of missing micro-pore structures on the core-scale CT images.

In this study, carbonate cores are collected from the Longwangmiao Formation in the Sichuan Basin, China, to analyze the structural features and mineral compositions, by using core-scale CT scans, cast thin sections (CTSs), and X-ray diffraction (XRD). Ultrasonic and low frequency testing with different pressures and fluids are conducted to investigate the acoustic responses of carbonate rocks with respect to different structural types and frequency ranges. The core-scale DRP is analyzed to compare with the experimental data. Numerical simulations, differential equivalent medium (DEM) theory and a squirt flow model are then used to characterize the multiscale pore structure and simulate how they affect acoustic wave propagation.

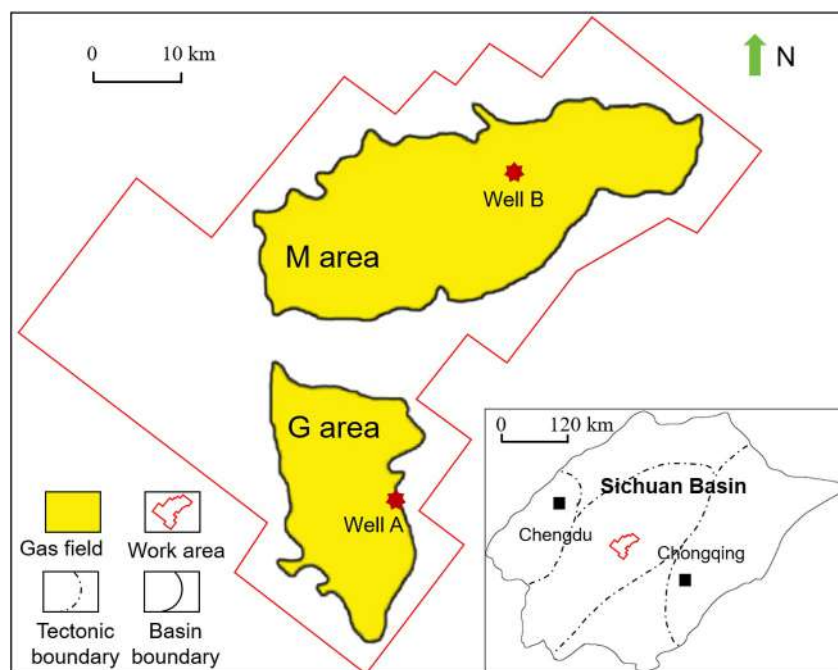


**Figure 1.** Schematic diagram of the study area. Wells A and B are indicated with stars.

## 2. Rock Samples and Laboratory Experiments

### 2.1. Reservoir Geology and Rock Specimens

This study focuses on a carbonate reservoir of the Longwangmiao Formation in the G-M area, Sichuan Basin, as is shown in Figure 1. The depth of the formation in this area is generally more than 4 km, the temperature is about 120°C, the overburden pressure is about 110 MPa, and the pore pressure is 65–70 MPa. The rock consists of pure dolomite with a very low proportion of clay minerals and has low porosity and permeability. The primary pore types are pores, caves, vugs and fractures, with gas and water being the main fluid types (Pang et al., 2019, 2024a).

To investigate the pore structure, we consider two wells (A and B) in the working area (G-M), and the reservoir porosity, gas saturation, P and S wave velocities, and density are shown in Figure 2, with the dashed red boxes representing the sampling locations. The six carbonate cores were taken from the target reservoir, Samples DS\_A-DS\_E and DS\_F from wells A and B, respectively. The two logs belong to the same stratigraphy and have the same lithology, which is why, the six samples are examined together in this work. We measure the porosities and permeabilities of the samples by using the automatic permeameter of the core measurement system. Table 1 contains detailed information on the sampling depths, and lithology and physical parameters of the samples. Samples DS\_A-DS\_E have a lower porosity (less than 5%) than sample DS\_F, which is consistent with the interpretations of the logs (Figure 2).

These cores were processed into cylinders with a diameter of 37.92–37.95 mm and a length of 49.48–50.56 mm and examined in the laboratory, including XRD, CTS, CT scan and ultrasonic measurements of P- and S-wave velocities as well as low-frequency measurements in relation to different pressures and fluids. These tests were designed to evaluate the lithology, mineral composition, pore structure and elastic wave properties of the carbonates.

### 2.2. XRD, CTS and CT Scans

XRD tests are carried out on the rock samples to analyze the mineral composition. This shows that dolomite (>98%) predominates with a very low proportion of clay minerals. Thin sections and CT scans are carried out to illustrate the rock structures. The CTSs of samples DS\_B, DS\_D and DS\_E are shown in Figure 3. The rock images show that the storage spaces in these rocks consist mainly of intergranular pores, dissolved caves and

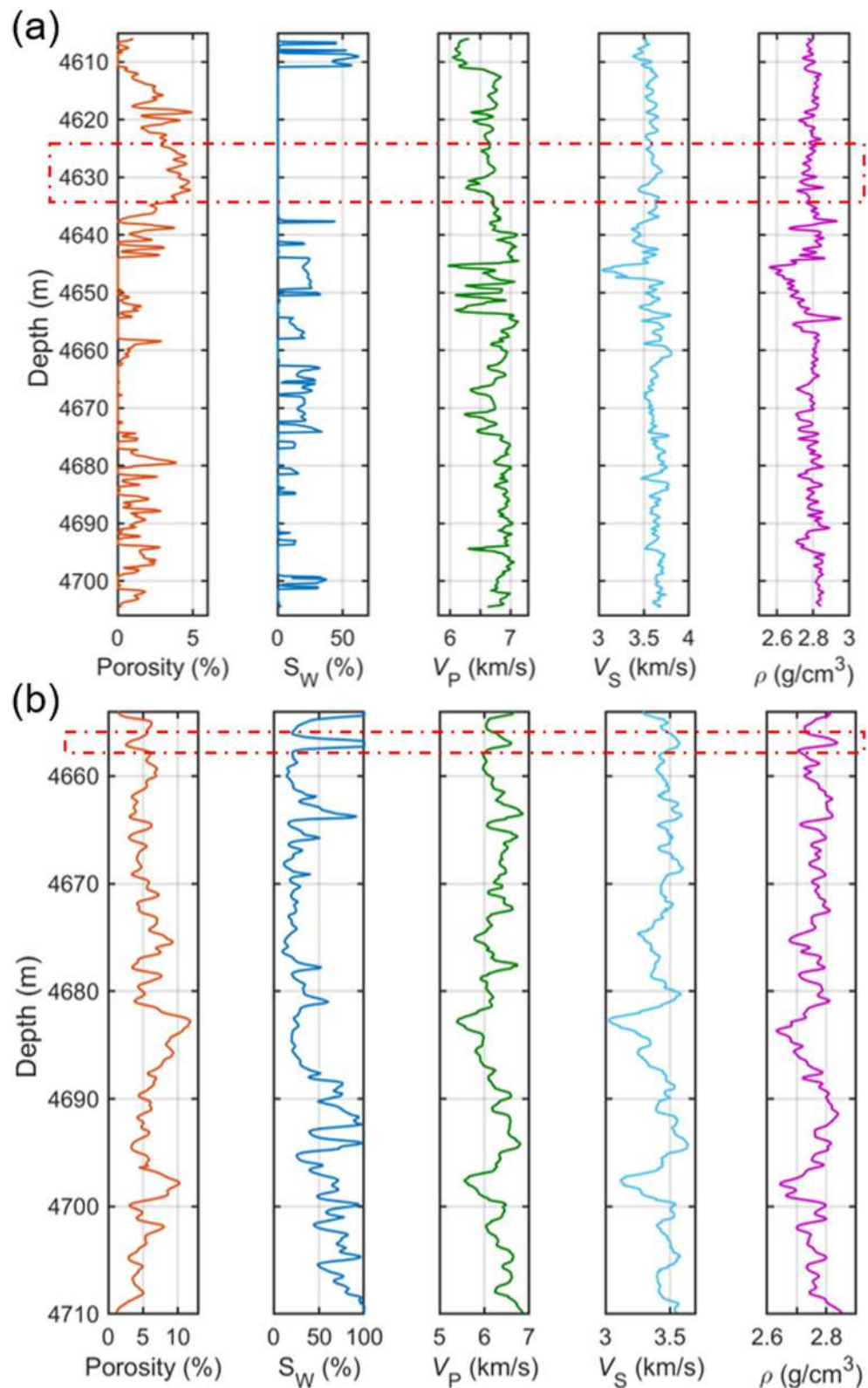
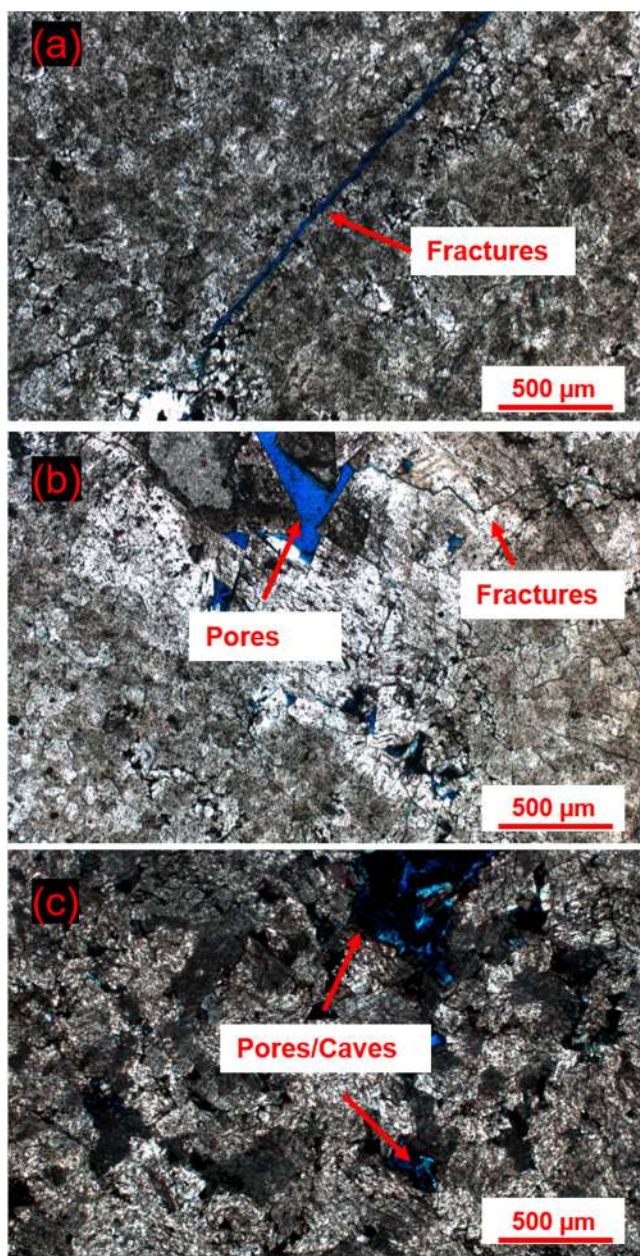


**Figure 2.** Log data from Wells A (a) and B (b). Left to right: porosity, water saturation, P-wave velocity, S-wave velocity, and density. The dotted red boxes indicate the sample collection locations.

**Table 1**  
*Physical Properties of Samples*

Samples	DS_A	DS_B	DS_C	DS_D	DS_E	DS_F
Lithology	Dolomite	Dolomite	Dolomite	Dolomite	Dolomite	Dolomite
Depth(m)	4,634.3	4,627.15	4,626.8	4,626.8	4,625.6	4,656.7
Porosity (%)	1.91	1.96	2.46	2.81	3.46	3.52
Permeability (mD)	0.001	0.159	0.135	0.141	0.001	0.088
Dry-rock density (g/cm <sup>3</sup> )	2.786	2.798	2.761	2.753	2.734	2.679



fractures. DS\_B shows predominantly fractures and fewer pores, DS\_D shows a combination of fractures and pores, while DS\_E shows more pores and caves.

The samples are then scanned in their total size, as are shown in Figures 4 and 5, with a voxel resolution of  $27.6 \times 27.6 \times 27.6 \mu\text{m}$ . The CT data sets provided are in 16-bit format, resulting in grayscale intensities ranging from 0 to 65,535. The intensity of the gray scale indicates phases with different absorption coefficients. Thus, lower absorption coefficients appear as black tones, like the pore space, and minerals appear as white tones, like dolomite. It can be observed that the rocks have different structures and pore types (Figures 4 and 5), which is consistent with the results of the thin sections (Figure 3). The thin sections show that the rocks have different pore structures, and the results of the 3D scan further confirm these findings. In this study, the samples (DS\_B), (DS\_A, DS\_C and DS\_D) and (DS\_E and DS\_F) are classified as fractured, fractured-vuggy and pore-cavity types, respectively, based on the images.

### 2.3. Ultrasonic and Low-Frequency Tests

#### 2.3.1. Experimental Conditions

Ultrasonic (1 MHz) and low-frequency (1–100 Hz) tests are carried out with different pressures and fluids to measure the wave velocities. To achieve a dry state (with air), the samples are first dried and then moistened in a sealed container. For the wet state, the sample is first immersed in a tank of water so that it is spontaneously saturated. To ensure complete saturation with water, the air is extracted and then the water pressure is increased to fill the pore spaces. Multi-frequency band wave measurements are performed at a temperature of about 25°C, a pore pressure of one atm and effective (confining minus pore) pressures from 1 to 50 MPa (which includes the in-situ conditions) for ultrasonic testing and 1–25 MPa for low frequency testing.

#### 2.3.2. Experimental Apparatus

Figure 6 shows the apparatus. The axial load, the confining pressure and the pore pressure in the upper and lower inlets are controlled by the pumps. The device is able to measure the elastic moduli and Poisson's ratio of the sample at different frequencies with a piezoelectric oscillator (Borgomano et al., 2020; Sun et al., 2022). The sample is held between the two aluminum end plates with four axial strain gauges to accurately determine the axial stress (Figure 6). The sample is encased in a neoprene jacket to isolate the pore fluid from the surrounding oil (Spencer, 1981). In addition, the P and S wave velocities are measured with the ultrasonic transducers (P and S

**Figure 3.** Thin sections of the samples DS\_B (a), DS\_D (b), and DS\_E (c).

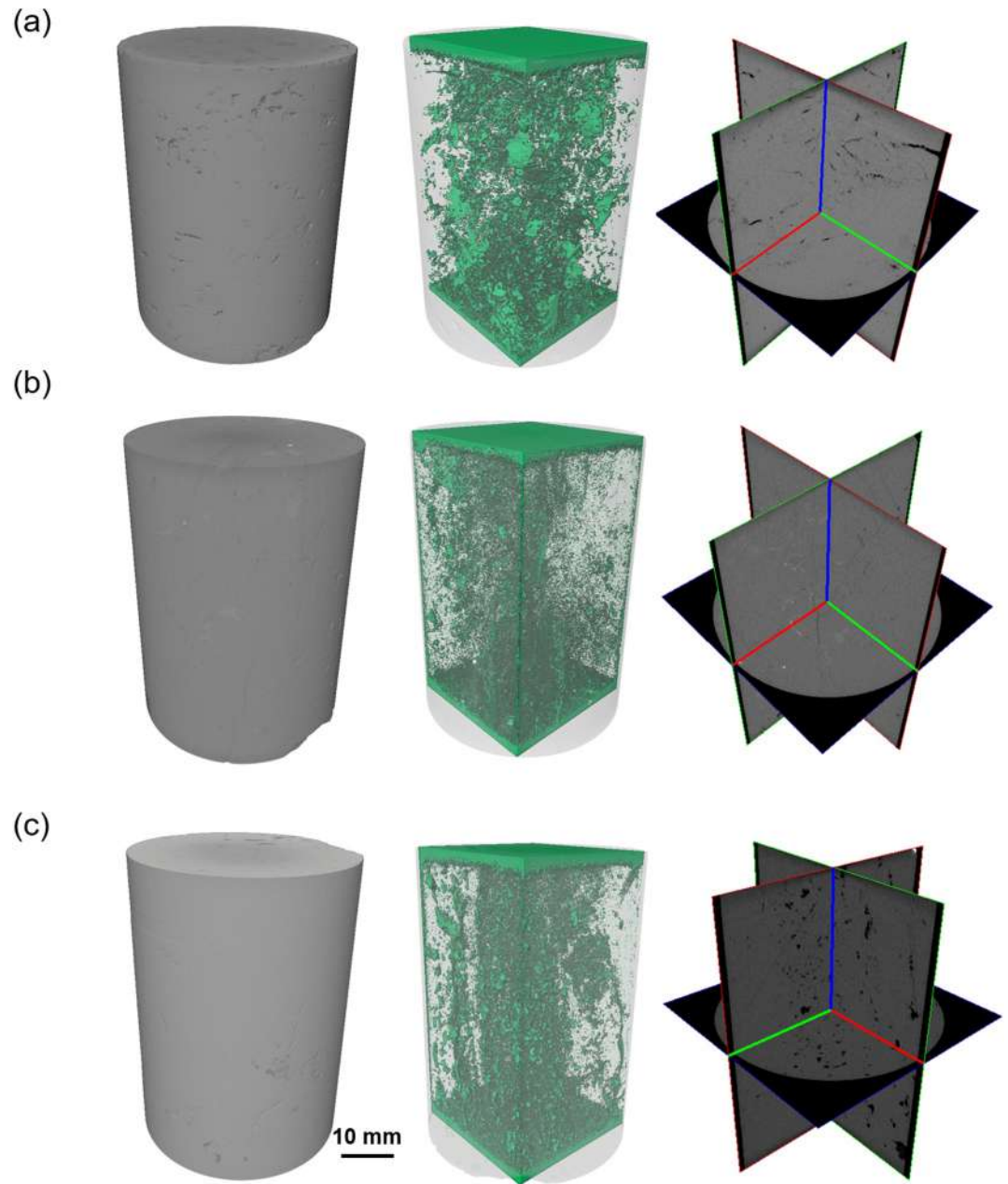


**Figure 4.** Computed tomography scan data and pore structures of the samples DS\_A (a), DS\_B (b), and DS\_C (c).

embedded in both end plates (1 MHz). The pore pressure can be controlled by the pumps attached to the end plates.

### 2.3.3. Measurements

First, ultrasound tests (1 MHz) are performed at both saturated states. The ultrasonic waveforms passing through the samples are recorded under the above conditions. The first incoming waves are extracted to compute the velocities of the P and S waves at different effective pressures (1–50 MPa and 11 points per sample).

Subsequently, low frequency tests (1–100 Hz) are performed in both saturated cases to measure the frequency-dependent Young's modulus and Poisson's ratio using the forced oscillation apparatus. The samples are connected to aluminum standards and axial stress oscillations generated by a piezoelectric transducer are applied. Strain

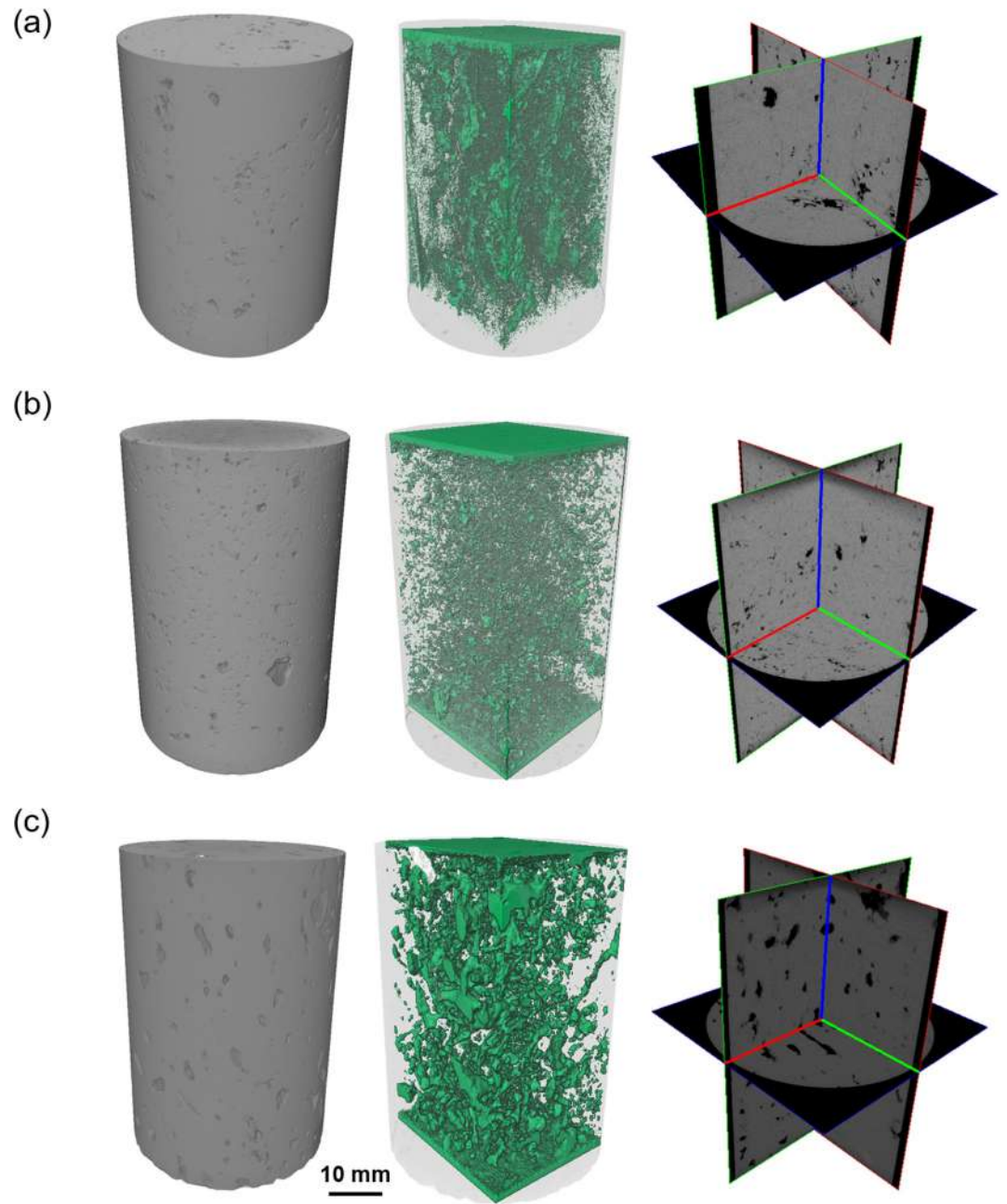


**Figure 5.** Computed tomography scan data and pore structure of the samples DS\_D (a), DS\_E (b), and DS\_F (c).

gauges record axial and radial strain amplitudes. In this way, the modulus of elasticity ( $E$ ) and Poisson's ratio ( $\nu$ ) are determined at different limiting pressures (1–25 MPa and 8 points per sample),

$$E = E_{Al} \frac{\epsilon_{ZZ}^{Al}}{\epsilon_{ZZ}}, \quad (1)$$

$$\nu = \frac{\epsilon_{rad}}{\epsilon_{ZZ}}, \quad (2)$$

where  $E_{Al}$  and  $\epsilon_{ZZ}^{Al}$  are Young's modulus and the measured longitudinal strain of the standard aluminum, and  $\epsilon_{ZZ}$  and  $\epsilon_{rad}$  are the axial and radial strains of the sample, respectively.

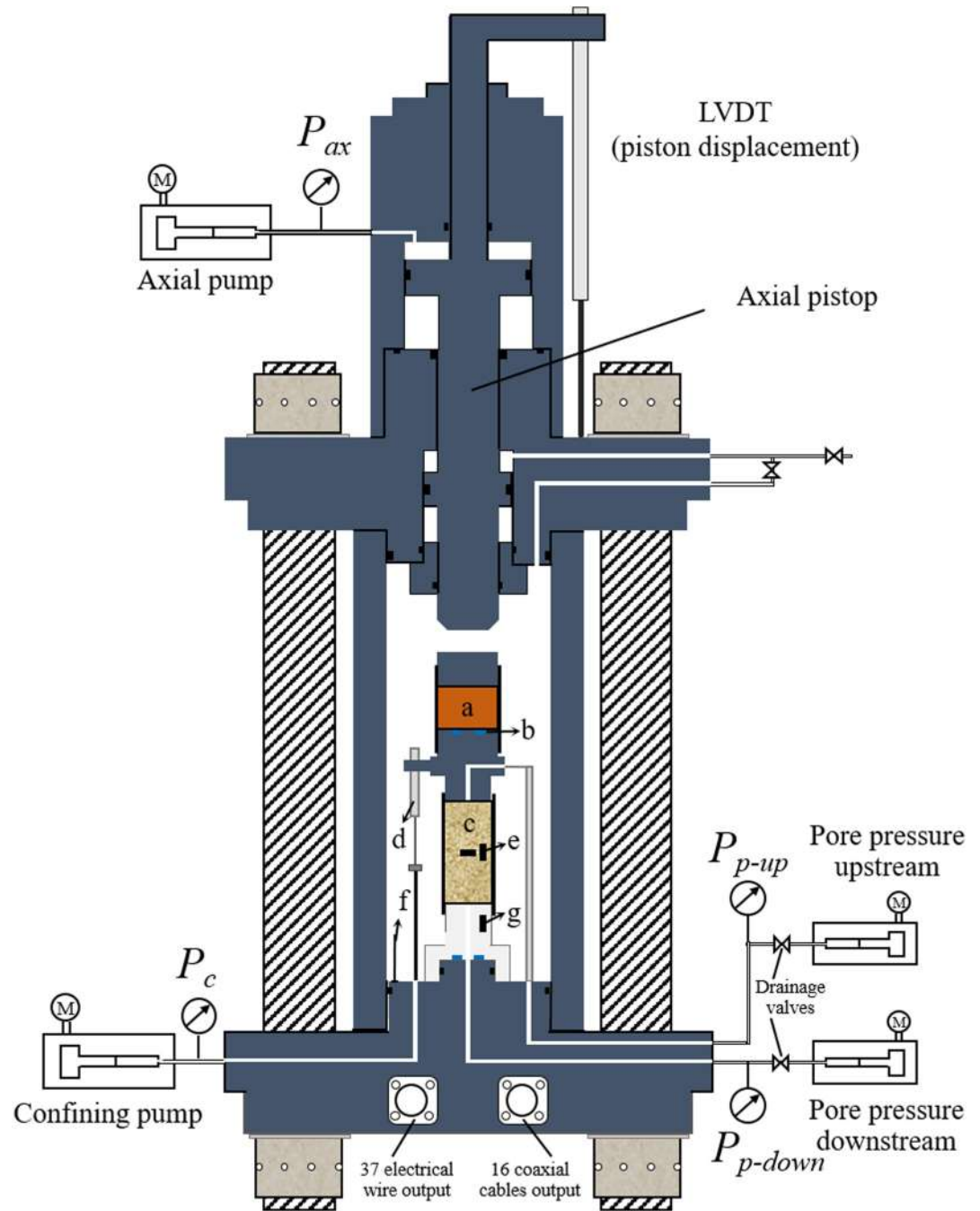


**Figure 6.** Ultrasonic and low-frequency experimental apparatus (modified after Borgomano et al. (2019)): (a) Piezoelectric oscillator (0–100 Hz); (b) P- and S-ultrasonic transducers; (c) rock sample; (d) internal linear variable displacement transducer (LVDT, global strain); (e) axial and radial strain gauges (sample); (f) thermocouple; (g) axial strain gauges (aluminum).

Then, the Bulk and Shear Moduli of the Samples Are

$$K = \frac{E}{3(1 - 2\nu)}, \quad (3)$$

$$G = \frac{E}{2(1 + \nu)}, \quad (4)$$

respectively, and the P- and S-wave velocities are

$$V_s = \sqrt{\frac{G}{\rho}}, \quad (5)$$

$$V_p = \sqrt{\frac{K + \frac{4}{3}G}{\rho}}, \quad (6)$$

respectively, where  $\rho$  is the mass density of the rock.

#### 2.4. Frequency-Dependent Velocities

The results of the ultrasound tests follow. Figures 7 and 8 show the P- and S-wave velocities ( $V_p$ ,  $V_s$ ) as a function of the effective pressure under gas-saturated and water-saturated conditions. The scatter shapes represent the different samples. The results show that the velocities generally increase with pressure, which is due to the closure of microcracks.  $V_p$  is higher under wet conditions than that under gas-saturated conditions due to the larger bulk modulus of water, which increases the stiffness and velocity of the rock. In addition, the fluid (water) flow leads to wave dispersion, resulting in a greater difference in velocity between water and gas saturated conditions.  $V_s$  is lower in the wet state, which is due to the increasing rock density with water saturation, while the shear modulus remains unchanged according to the Gassmann equation (Gassmann, 1951).

It can also be seen that the pressure dependence of the samples is different, with DS\_A, DS\_C, and DS\_D showing large fluctuations with pressure, while DS\_E and DS\_F show relatively small fluctuations. Sample DS\_F (with the highest porosity) is the least sensitive to pressure, and the velocity of the sample reaches a nearly constant value when the pressure is above 20 MPa. It can be concluded that the pressure dependence of the samples is significantly influenced by the pore structure and pore type.

The elastic responses of the samples in the low frequency range (1–100 Hz) are shown in Figures 9–12. They show the velocity variations with frequency in relation to different pressures (1–25 MPa) and fluid types (gas or water). The velocities increase with pressure for both saturation states and show a similar trend to the ultrasonic results.  $V_p$  in the gas-saturated state and  $V_s$  are almost constant with frequency variations, while  $V_p$  in the wet state increases with frequency. The velocity dispersion result is due to the fluid flow caused by the elastic wave passing through water-saturated porous rock. It can also be seen that the frequency dependence of the elastic properties shows a different behavior at variable pressure: the higher the pressure, the lower the dispersion. Samples DS\_B and DS\_F show almost no variation with frequency at the high pressure (25 MPa), indicating that rocks with different pore structures have different sensitivity to pressure, which is consistent with the ultrasonic results (Figures 7 and 8).

Based on the low-frequency and ultrasonic measurements, the elastic wave responses of samples within multi-frequency bands can be analyzed by extracting the data at an effective pressure of 1 MPa, as are shown in Figures 13 and 14.  $V_p$  increases with frequency at the wet state and is higher in the ultrasonic frequency range compared to lower band, while  $V_p$  in the gas-saturated state and  $V_s$  are almost unchanged.

#### 2.5. Elastic Properties and the Pore Structure

The measurements also show the large difference in elastic properties between the samples. The ultrasonic velocity at 1 MPa as a function of porosity is shown in Figure 15. It can be seen that there is no reasonable relationship between the velocity and porosity, with DS\_E and DS\_F with higher porosity showing even higher velocities. In particular, DS\_F (with the highest porosity) has the highest velocity and DS\_A (with the lowest porosity) shows the lowest velocity, which contradicts conventional measurements and findings and shows that porosity is not the main factor controlling these attributes for the tight carbonates.

In Section 2.2, we classified the samples into three types based on the CT scan and thin sections: fractured (DS\_B), fractured-vuggy (DS\_A, DS\_C, DS\_D), and pore-cavity (DS\_E, DS\_F), which are represented by different colors in Figure 15. From this point of view, the rock types with pore cavities have higher velocities, while the fractured-vuggy have lower velocities. The fractured type has a high  $V_p$  and a relatively low  $V_s$ . In the

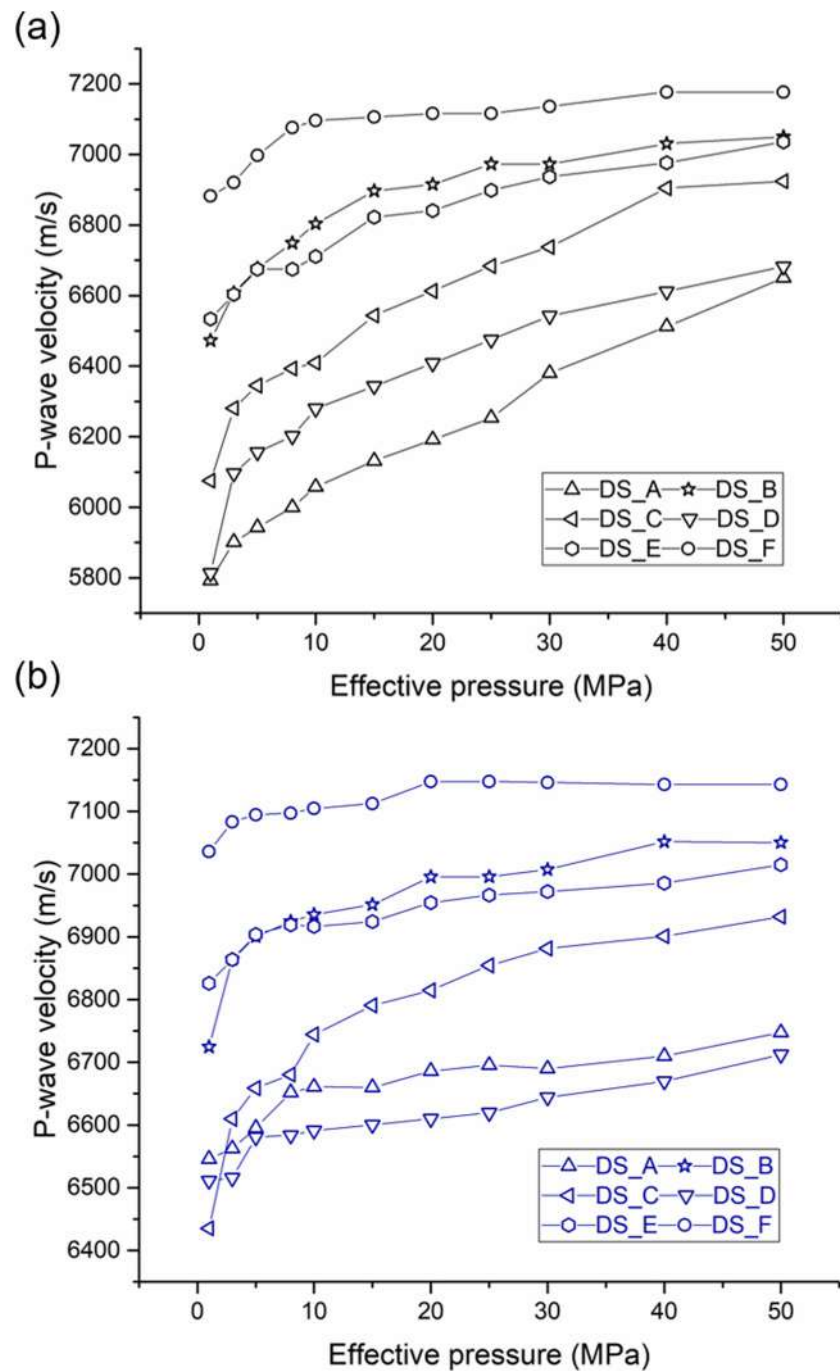


**Figure 7.** Ultrasonic P-wave velocity as a function of effective pressure at gas-saturated (a) and water-saturated (b) states.

area of very low porosity, the pore structure becomes the dominant factor in the wave properties. For rocks with pore cavities, DS\_F with higher porosity has a higher velocity than DS\_E, which could be associated with different pore/fracture characteristics.

The laboratory experiments show that carbonates have complex pore structures that have a considerable influence on the elastic parameters. In order to interpret the complex petrophysical properties, a DRP analysis is performed to observe and characterize the rock structure.

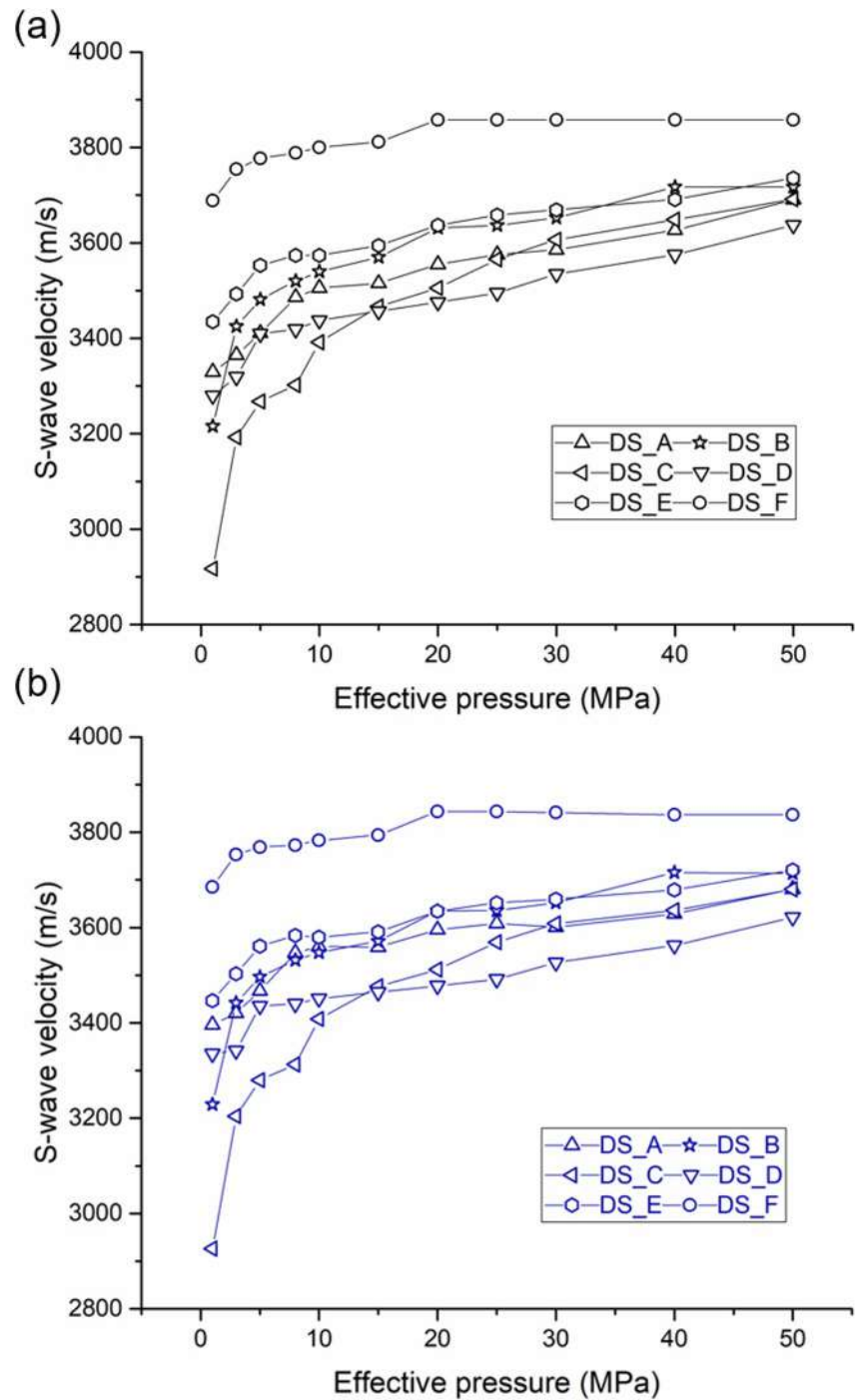


**Figure 8.** Ultrasonic S-wave velocity as a function of effective pressure at gas-saturated (a) and water-saturated (b) states.

### 3. Digital Rock Physics

In this work, 3D digital rock is reconstructed by using CT scan data, thin sections (which can help in creating the digital cores by observing mineral grain sizes), and XRD mineral analysis, to create a pore network model and derive structural parameters such as pore radius and shape factor. Then, we simulate the effective elastic velocities by using a FD method with rotated staggered grids.

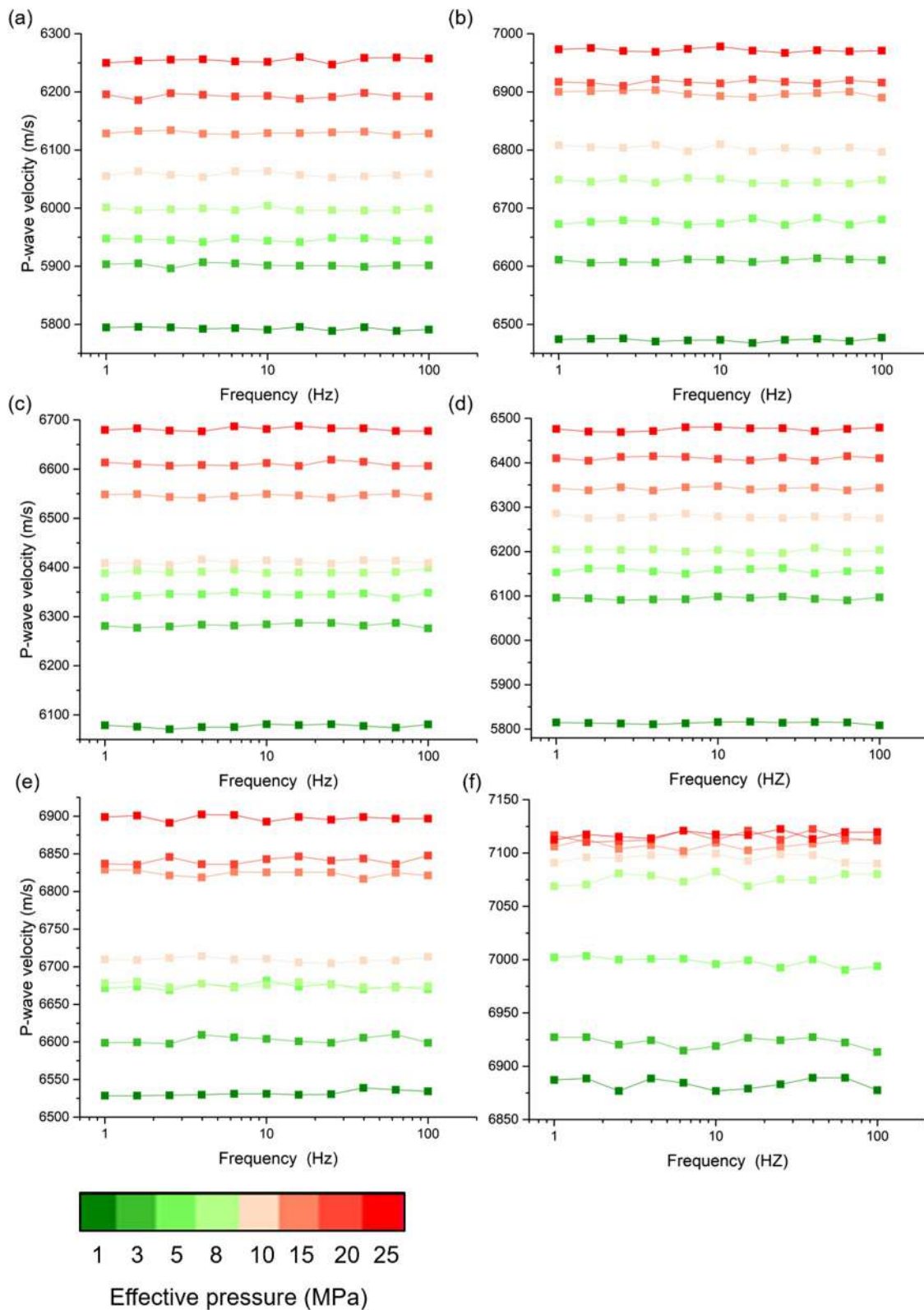


Figure 9. P-wave velocity as a function of frequency at different pressures at gas-saturated state. (a), DS\_A; (b), DS\_B; (c), DS\_C; (d), DS\_D; (e), DS\_E; (f), DS\_F.

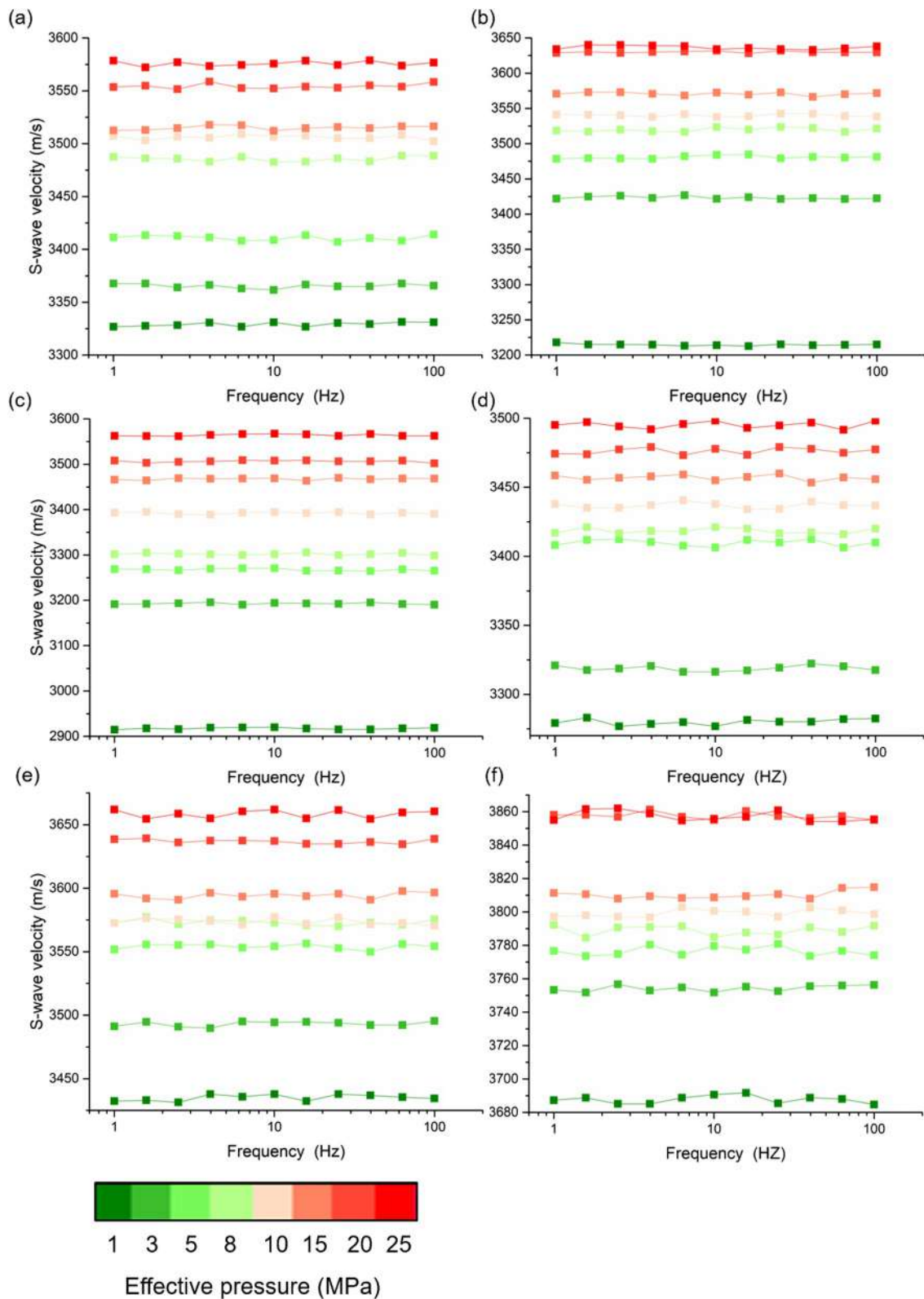


Figure 10. S-wave velocity as a function of frequency at different pressures at gas-saturated state. (a), DS\_A; (b), DS\_B; (c), DS\_C; (d), DS\_D; (e), DS\_E; (f), DS\_F.

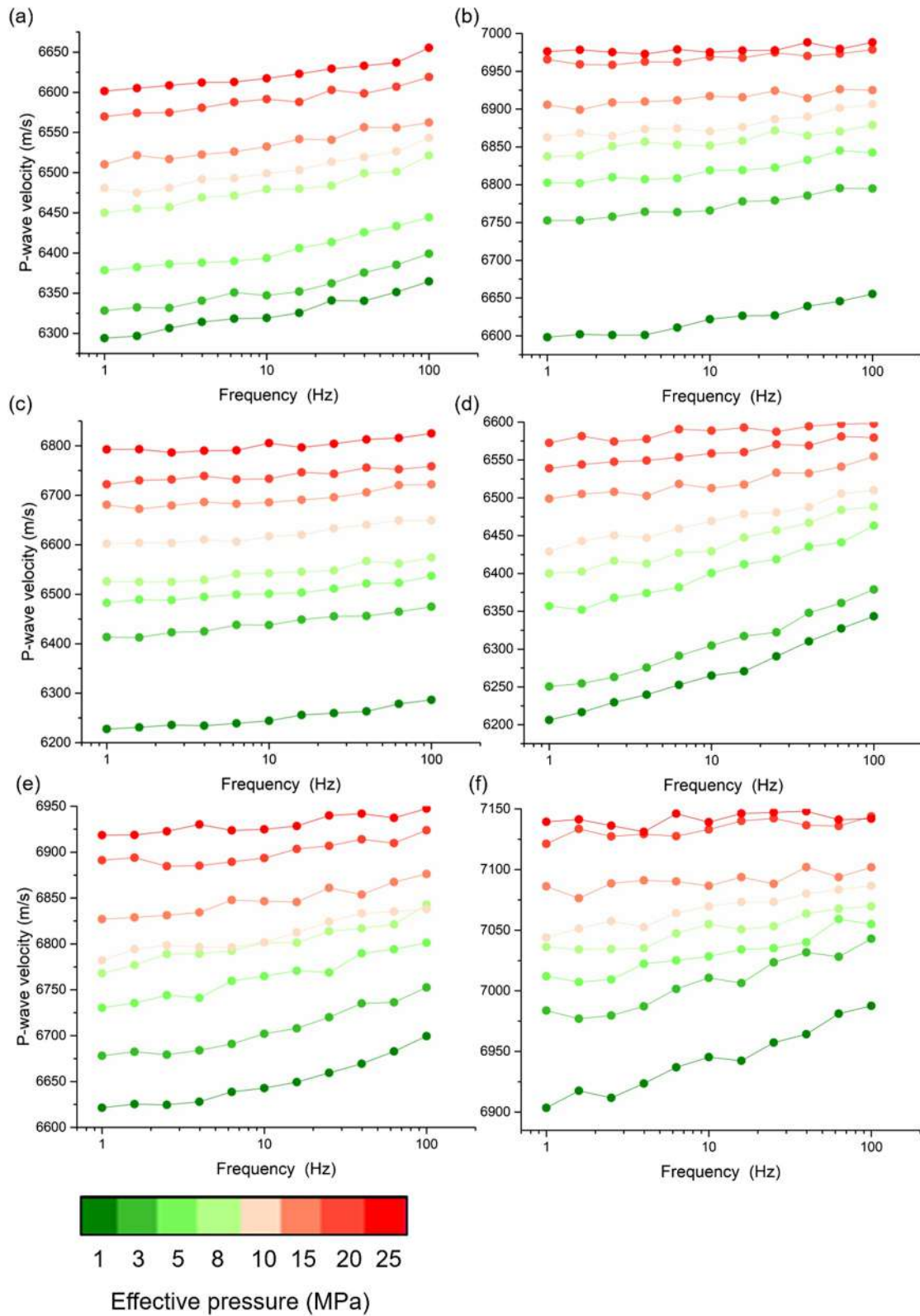


Figure 11. P-wave velocity as a function of frequency at different pressures at water-saturated state. (a), DS\_A; (b), DS\_B; (c), DS\_C; (d), DS\_D; (e), DS\_E; (f), DS\_F.

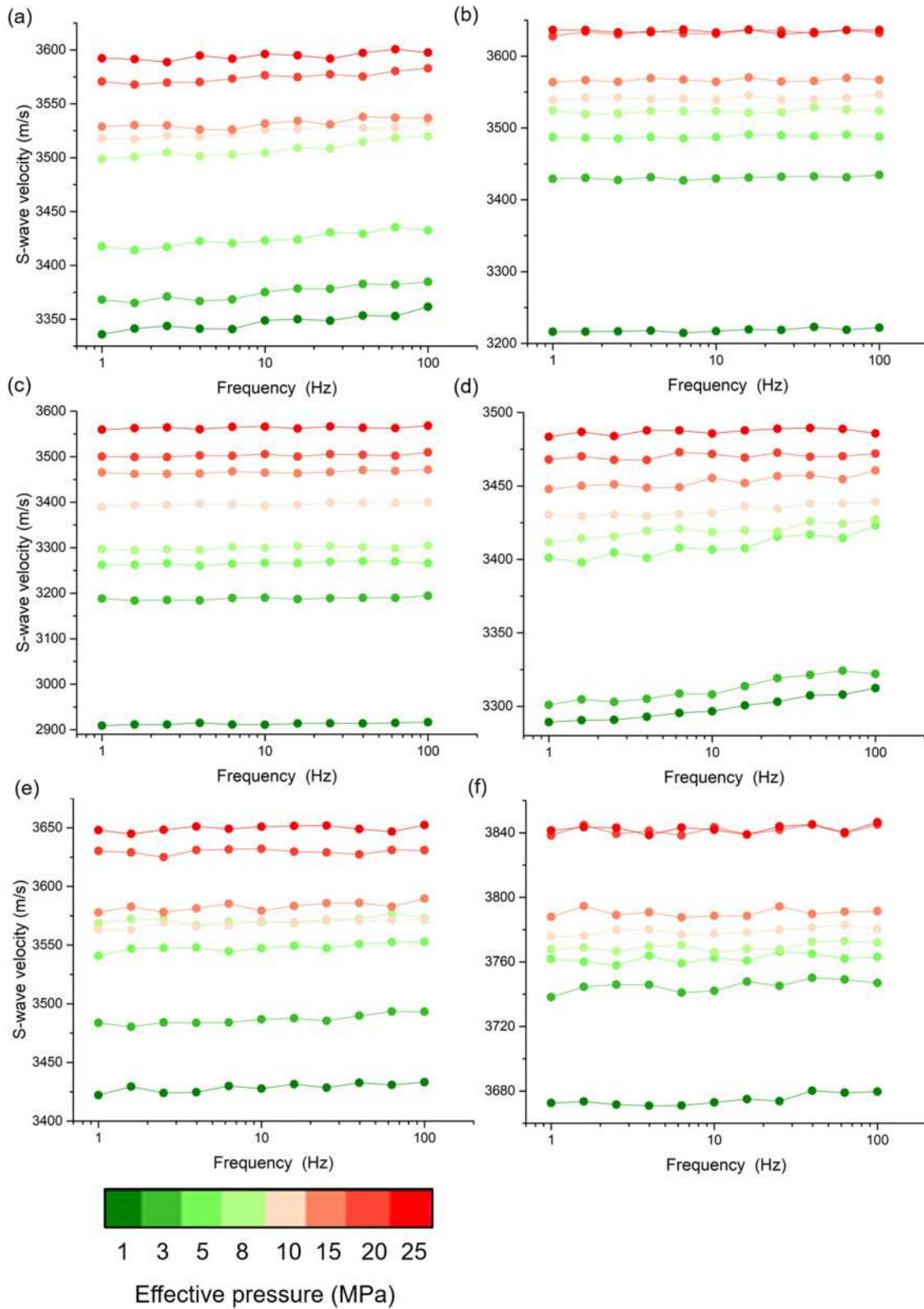
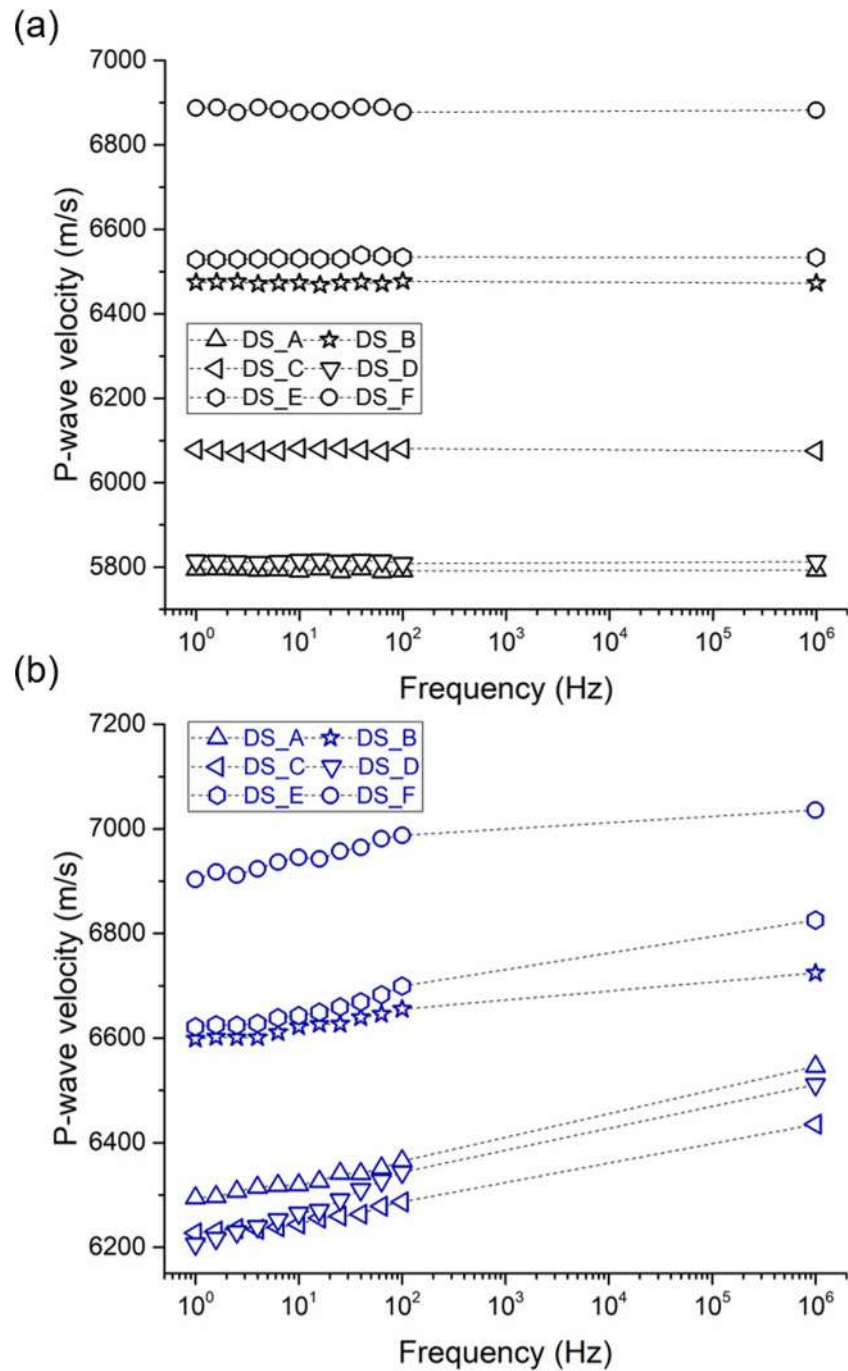


Figure 12. S-wave velocity as a function of frequency at different pressures at water-saturated state. (a), DS\_A; (b), DS\_B; (c), DS\_C; (d), DS\_D; (e), DS\_E; (f), DS\_F.



**Figure 13.** P-wave velocity as a function of frequency for the samples at 1 MPa effective pressure at gas-saturated (a) and water-saturated (b) states.

### 3.1. Digital Rocks and Pore Structure

The digital cores are created by numerical segmentation of the rock images. First, a non-local-mean filter is used for denoising. A threshold segmentation workflow is then applied based on the individual and repeated application of the grayscale threshold for each stage, minimizing the critical boundary regions in the grayscale histogram near two peaks that ideally reflect the phase attenuation coefficients (Pang et al., 2024b). Segmentation takes into account geological diagenesis, mineral composition, sample microstructure and porosity. It is assumed that the representative element volume (REV) can be used to analyze the rock properties (Karimpouli et al., 2023;

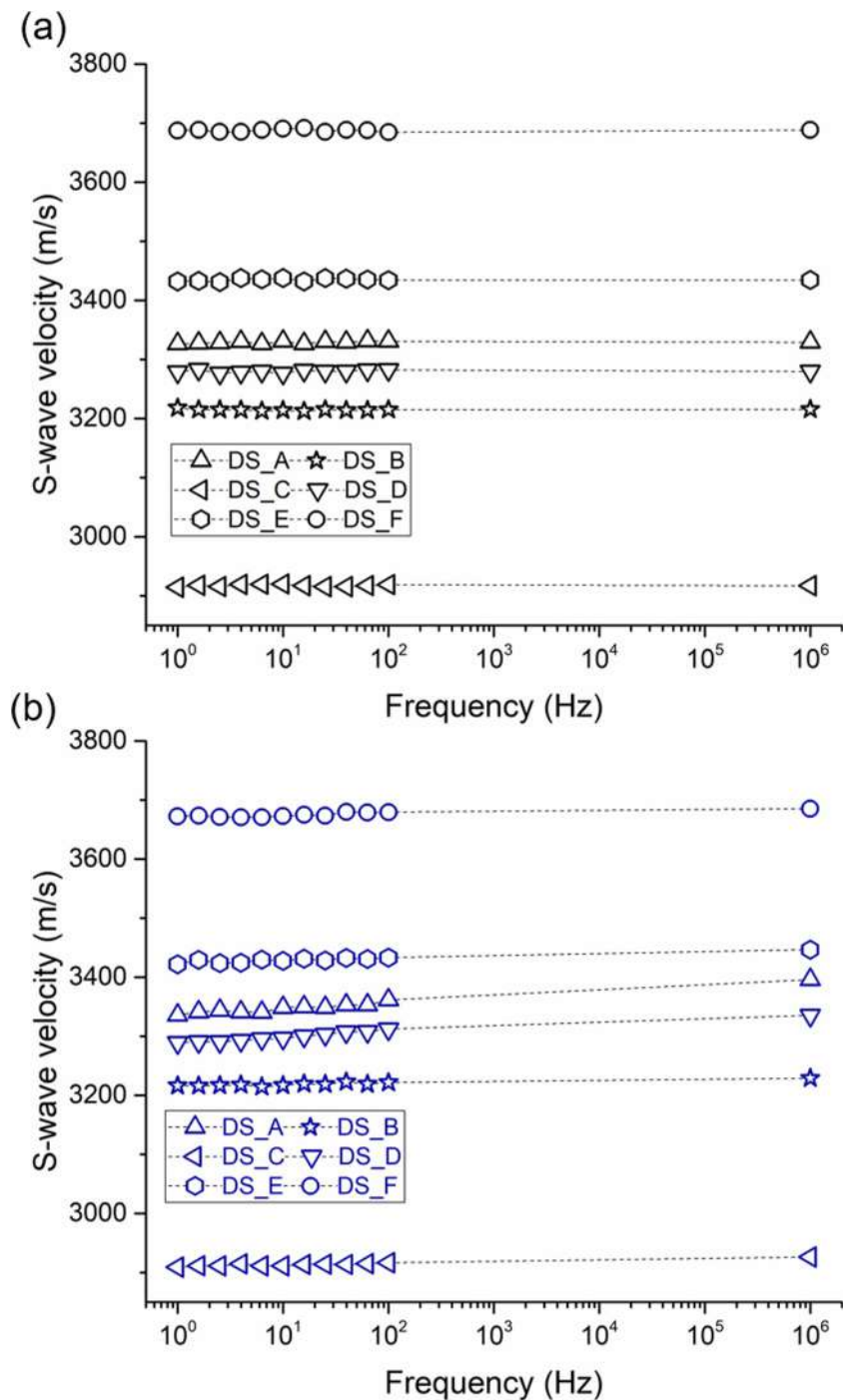


**Figure 14.** S-wave velocity as a function of frequency for the samples at 1 MPa effective pressure at gas-saturated (a) and water-saturated (b) states.

Saxena et al., 2019; Siegert et al., 2022). Subsequently, the REV is selected to achieve a suitable size that allows accurate characterization of the rock microstructure while meeting the storage and computational requirements. In addition to satisfying these two conditions, the porosity results are also used as constraints to obtain the appropriate REV.

The digital models in this work comprise a cube of  $400^3$  voxels (Figure 16) divided into pore and mineral phases (dolomite and clay); the determined volume fractions of the phases are given in Table 2. The rock is dominated by

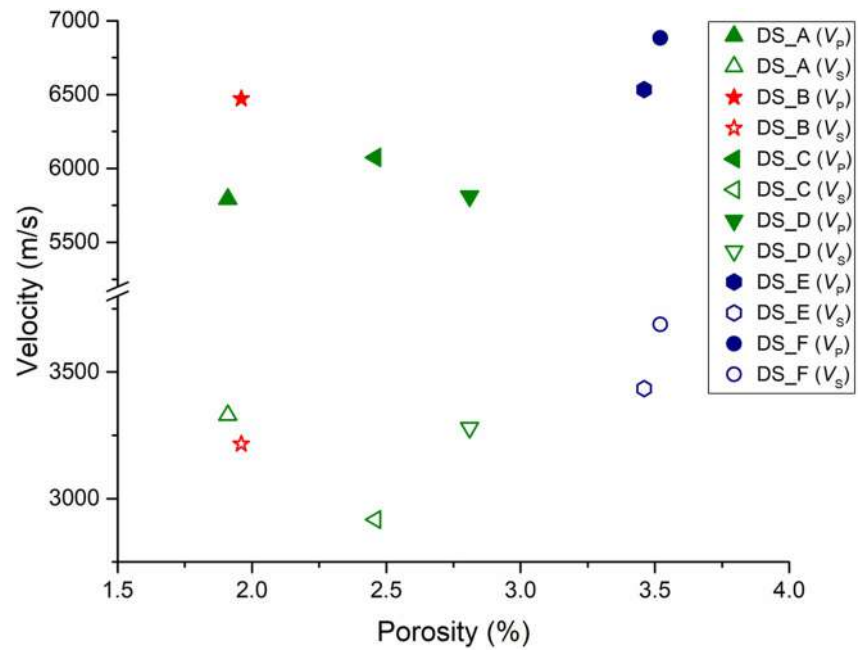


**Figure 15.** Elastic velocities as a function of porosity at 1 MPa effective pressure at gas-saturated state. The solid and empty scatters are the P- and S-wave velocities, respectively.

the mineral dolomite and has a very low clay content. The segmented porosity is generally higher than the measured porosity (with the exception of DS\_E), which could be due to the presence of isolated pores. Furthermore, the segmented porosity here refers to pores within the local area of small sizes of the selected

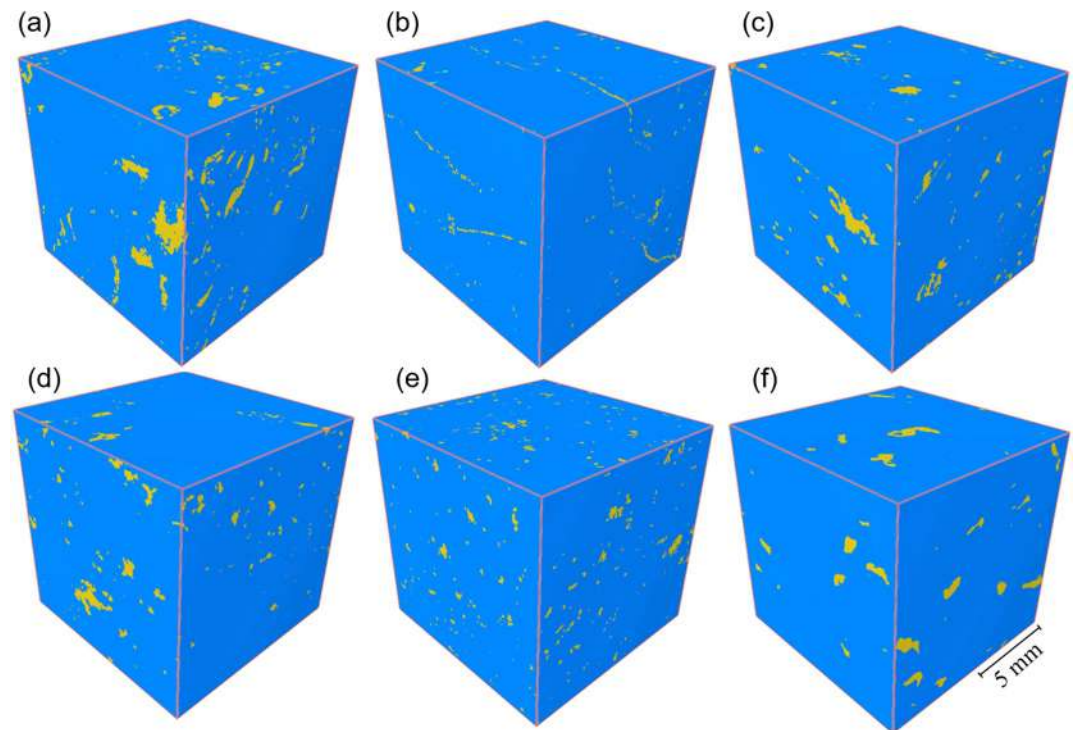


**Figure 16.** Determined digital rocks based on the segmentation approach. The blue and yellow represent dolomite and pore, respectively. The clay phase (green) is too small to be distinguished in the figure. (a), DS\_A; (b), DS\_B; (c), DS\_C; (d), DS\_D; (e), DS\_E; (f), DS\_F.

**Table 2**  
Determined Phases Fractions Based on the Segmentation Approach

Samples	DS_A	DS_B	DS_C	DS_D	DS_E	DS_F
Porosity (%)	3.5236	1.996	2.9458	3.47	2.81	3.9087
Dolomite (%)	96.476	97.919	97.0542	96.53	97.1873	96.0747
Clay (%)	0.0004	0.085	0	0	0.0027	0.0166

et al., 2019; de Vries et al., 2017; Lai & Wang, 2015; Zhu et al., 2023a). According to their views, this study considers the pore space recognized by CT scans as macro-pore structures (containing macroscopic pores and fractures), in addition, the undetected part is considered as microporous structures (including microscopic pores and cracks).

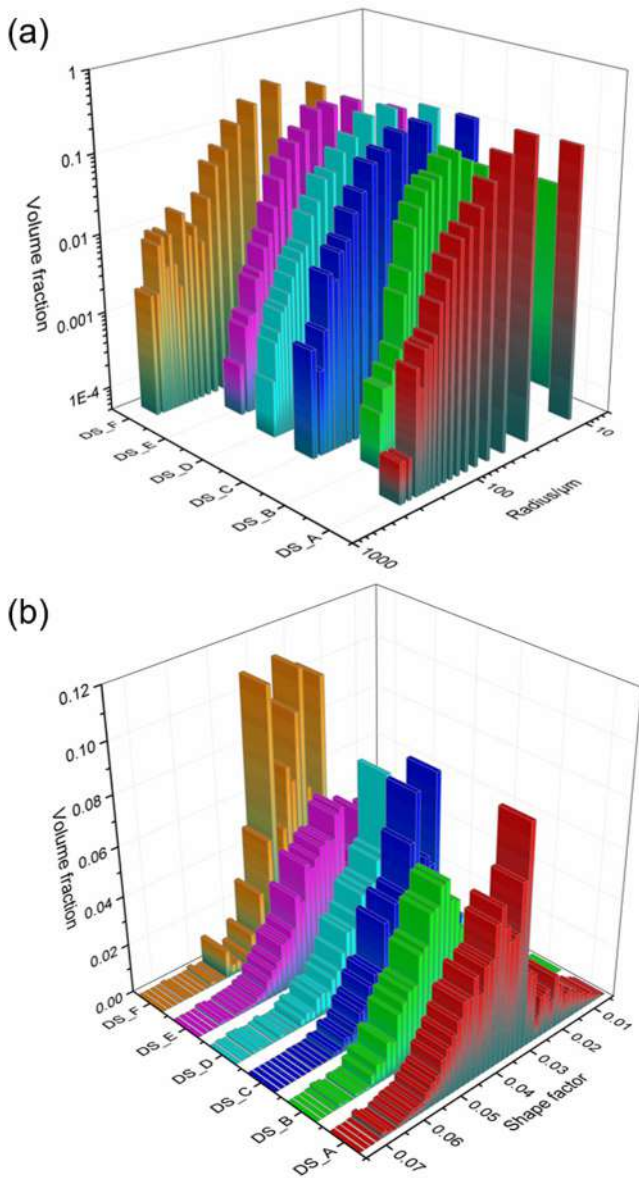


**Figure 17.** Pore radii and shape factors of the rock samples.

representative element, which could be another reason for the discrepancy. It has been shown that CT scans can cover the isolated pores (Bazaikin et al., 2017; Latief & Feranie, 2014; Li et al., 2022), which are difficult to measure due to the complexity of the tight rocks.

After segmentation, the pore spaces are determined, which allows us to characterize pore-structure parameters. It should be clarified that the structure here refers to the macroporous structures. Previous studies have classified pore structures into macropores and micropores based on CT scans (Bailey et al., 2019; de Vries et al., 2017; Lai & Wang, 2015; Zhu et al., 2023a). According to their views, this study considers the pore space recognized by CT scans as macro-pore structures (containing macroscopic pores and fractures), in addition, the undetected part is considered as microporous structures (including microscopic pores and cracks).

Figure 17a shows the pore radii of the samples, which have different radius sizes. DS\_F shows a larger radius and DS\_B has a smaller radius. Figure 17b shows the shape factor, which indicates how close a pore is to a sphere (e.g. an ideal sphere has a shape factor of 1). The shape factor is calculated based on the surface area and volume of the pores (Lv et al., 2020; Qin et al., 2022),

$$SF = \frac{36\pi V_{\text{pore}}^2}{S^3}, \quad (7)$$

where SF is the shape factor, and  $V_{\text{pore}}$  and  $S$  stand for the volume and surface area of the pore, respectively. The shape factors are small, indicating that the pores are irregular in geometry.

Next, the maximal ball algorithm is used to create regularized pore-throat models (Al-Kharusi & Blunt, 2007) that represent the pore spaces and structural properties, as shown in Figure 18. The sphere represents the pores, and the capillaries denote the throats and fractures. It can be observed that DS\_B (fractured type) contains more developed throats and smaller pores, DS\_A, DS\_C, and DS\_D (fractured-vuggy type) have developed pores and fractures, DS\_E and DS\_F (pore-cavity type) have many pores and fewer throats, and DS\_F has significantly larger pore radii. This is consistent with the behaviors shown in Figure 17a. In this way, the volume fractions of the macroscopic pores (stiff pores,  $\phi_{0,\text{macro}}$ ) and throats (fractures,  $\phi_{c,\text{macro}}$ ) can be obtained, as shown in Table 3.

### 3.2. Numerical Simulation

Computer simulations are applied to the wave responses based on the constructed 3D digital rocks. First, for the digital core, each phase is supplemented by the physical mineral properties according to Mavko et al. (2009), where the bulk and shear moduli and density of dolomite and clay are 94.9 GPa, 45 GPa, and 2.87 g/cm<sup>3</sup> and 21 GPa, 7 GPa, and 2.6 g/cm<sup>3</sup>, respectively. The content of clay minerals is extremely low, so that it hardly influences the elastic parameters in the actual simulation. To simulate the elastic wave propagation, we use an FD method with rotated staggered grids (Saenger & Bohlen, 2004; Saenger et al., 2000), as is shown in Figure 19. Here we consider the velocities of elastic waves propagating through a heterogeneous material at the long wavelength limit (the pore size is much smaller than the wavelength).

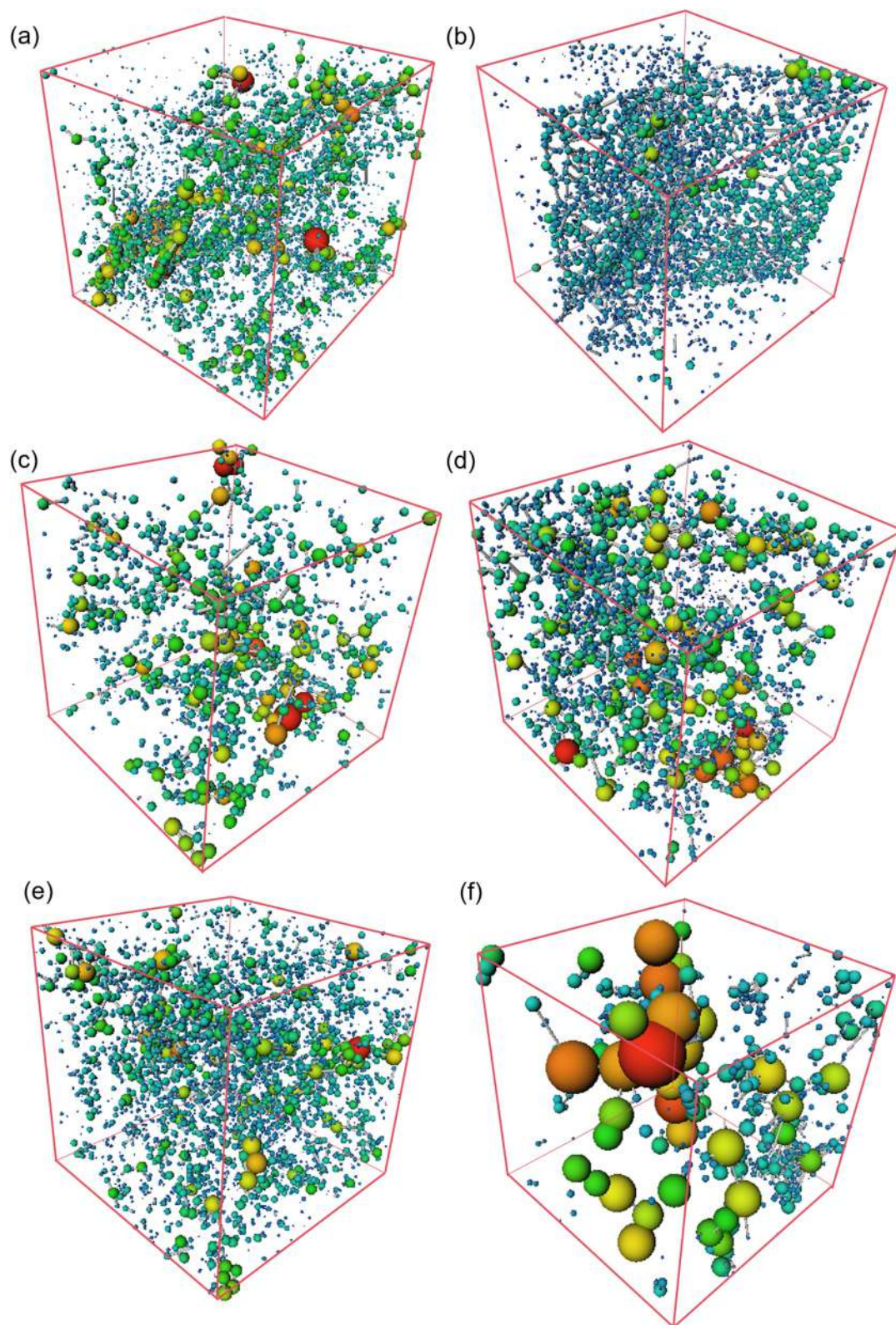


**Figure 18.** Pore network model of the carbonate samples. (a), DS\_A; (b), DS\_B; (c), DS\_C; (d), DS\_D; (e), DS\_E; (f), DS\_F. The ball colors (sizes) are indicating the pore size volumes.

**Table 3**  
Determined Volume Fractions of the Macro-Pores and Fractures

Samples	DS_A	DS_B	DS_C	DS_D	DS_E	DS_F
$\phi_{0,macro}$ (%)	2.685	1.282	2.225	2.65	2.266	4.584
$\phi_{c,macro}$ (%)	0.839	0.714	0.72	0.82	0.544	1.533

According to Saenger and Bohlen (2004), the effective elastic properties are determined by solving the elastic wave equations in the displacement-stress formulations,

$$\rho \frac{\partial^2 u_i}{\partial t^2} = c_{ijkl}^2 \frac{\partial^2 u_i}{\partial x_j^2} + f \quad (i = 1, 2, 3), \quad (8)$$

where  $u$  denotes displacement,  $\rho$  is density,  $c_{ijkl}$  is the elasticity tensor,  $f$  denotes the source,  $t$  is time and  $i$  indicate the subindices of the spatial variables.

Numerical simulations of the constructed digital cores are carried out, as are shown in Figure 20, which gives a snapshot of the 3D wavefield of the sample DS\_A. P- and S-wave velocities can be determined from the traveling time of the plane waves. The simulated results are compared with the ultrasonic measurements at different pressures, as are shown in Figure 21. The results show that the simulated velocities are generally higher than the measured ones, with DS\_A, DS\_C, DS\_D, and DS\_E having even higher velocities than those measured at the highest pressure. This discrepancy is attributed to the limited accuracy of the CT scan of the entire core, which does not capture some of the micro-pore structures, resulting in a higher velocity prediction.

#### 4. Reformulated Rock-Physics Model

To capture the undetected microscopic pore structure in core CT scans, we develop a reformulated RPM based on the numerical simulations with the theories of equivalent medium and squirt flow. The modeling procedure is shown in Figure 22. The combination of digital and theoretical rock physics enables the characterization of the multi-scale pores and the simulation of the effects of structure and fluid on the wave response characteristics.

The approach uses DRP to simulate the effective moduli considered for a rock skeleton with the large-scale pore structures. Microscopic pores and cracks are added using DEM theory to obtain a dry rock with the complete pore structures. Finally, the squirt flow model is applied to simulate the velocity and attenuation of the saturated rock.

The effective elastic moduli of rocks with larger pores and fractures are calculated with the simulated elastic velocities and rock density,

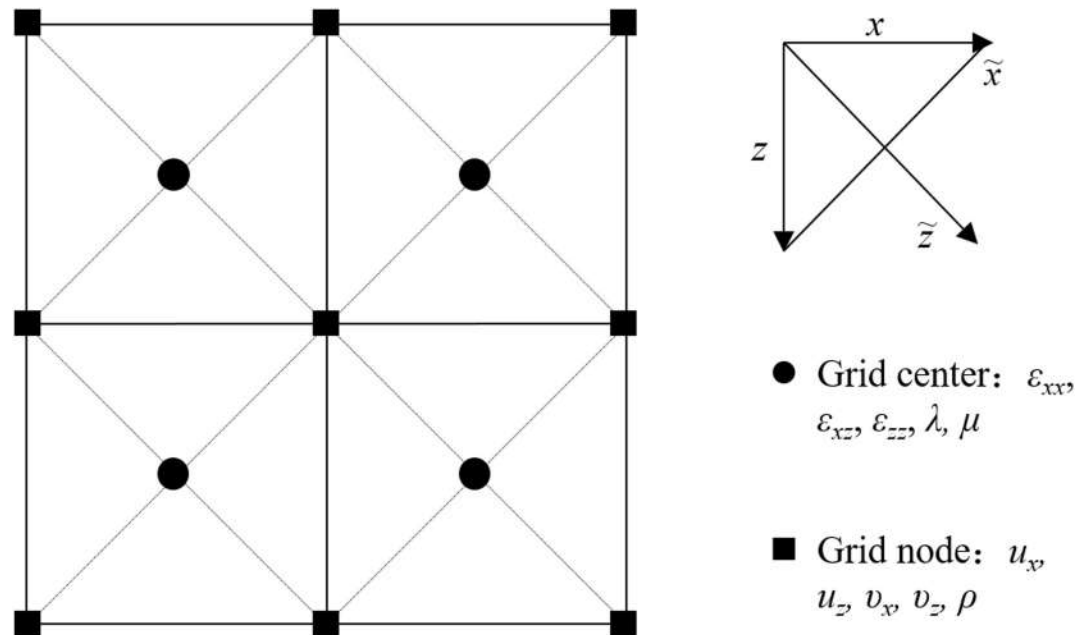


**Figure 19.** Elementary cells of the rotated staggered grid. Locations where strains ( $\epsilon_{xx}$ ,  $\epsilon_{xz}$ ,  $\epsilon_{zz}$ ), displacements ( $u_x$ ,  $u_z$ ), particle velocities ( $v_x$ ,  $v_z$ ), density ( $\rho$ ), and Lamé parameters ( $\lambda$ ,  $\mu$ ) are defined (see Saenger et al., 2000).

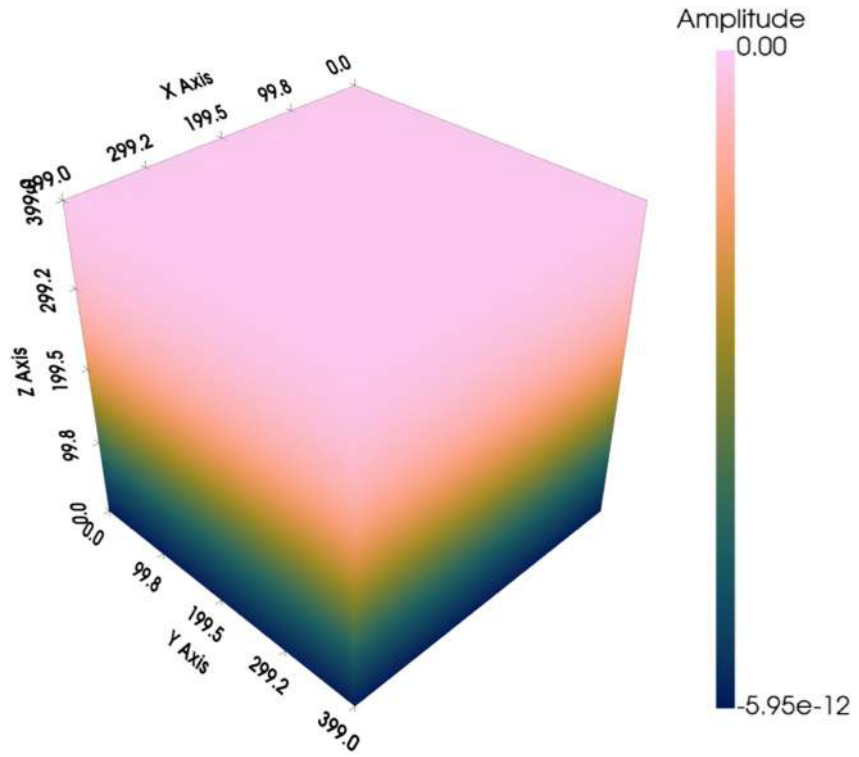


**Figure 20.** A snapshot of the 3D wavefield of the sample DS\_A.

$$G_{\text{eff}} = \tilde{V}_S^2 \rho_{\text{eff}}, \quad (9)$$

$$K_{\text{eff}} = \tilde{V}_P^2 \rho_{\text{eff}} \cdot \frac{4}{3} G_{\text{eff}}, \quad (10)$$

$$\rho_{\text{eff}} = \rho_s \cdot (1 - \phi_{\text{macro}}) + \rho_f \phi_{\text{macro}}, \quad (11)$$

where  $\tilde{V}_P$  and  $\tilde{V}_S$  are the simulated P- and S-wave velocities of the digital core, respectively,  $K_{\text{eff}}$  and  $G_{\text{eff}}$  denote the effective bulk and shear moduli, and  $\rho_f$ ,  $\rho_s$  and  $\rho_{\text{eff}}$  are the densities of the fluid, mineral and rock, respectively. The macroscopic porosity  $\phi_{\text{macro}}$  (which is the sum of macroscopic stiff porosity  $\phi_{0,\text{macro}}$  and fracture porosity  $\phi_{c,\text{macro}}$ ) of the digital sample is considered here.

Then the undetected microscopic pores/cracks of the CT scan are considered. We assume that the microscopic pore structure consists of a series of stiff and soft (crack) pores, which are equivalent ellipsoids with different aspect ratios. The DEM equations are then applied to successively input the microscopic pores and cracks into the effective moduli of elasticity from the simulations. The bulk and shear moduli of the dry rock ( $K_{\text{dry}}$  and  $G_{\text{dry}}$ ) with the multiscale pore structures can be determined with the DEM equations derived by Berryman (1992),

$$(K_2 \cdot K_{\text{dry}}^*) P^{(*2)}(y) = (1 - y) \frac{d}{dy} [K_{\text{dry}}^*(y)], \quad (12)$$

$$(G_2 \cdot G_{\text{dry}}^*) Q^{(*2)}(y) = (1 - y) \frac{d}{dy} [G_{\text{dry}}^*(y)], \quad (13)$$

with the initial conditions  $K_{\text{dry}}^*(0) = K_{\text{eff}}$  and  $G_{\text{dry}}^*(0) = G_{\text{eff}}$ , where  $K_{\text{eff}}$  and  $G_{\text{eff}}$  are the bulk and shear moduli of the host material (here, they are the effective moduli of the digital rock), respectively.  $y$  is the content of Phase 2 (microscopic pores  $\phi_{0,\text{micro}}$  or cracks  $\phi_{c,\text{micro}}$ ), and  $K_2$  and  $G_2$  are the corresponding bulk and shear moduli,

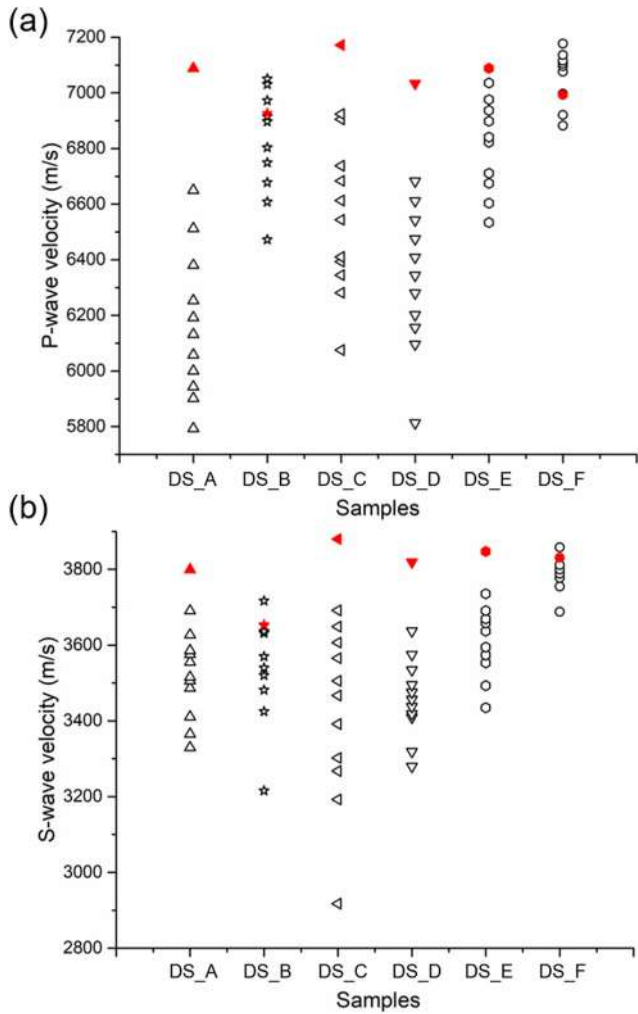


**Figure 21.** Simulation results (red) compared with the ultrasonic measurement data (black) at different effective pressures.

$\alpha_{c,micro}$  is the corresponding aspect ratio.  $J_0$  and  $J_1$  are the 0th and 1st order Bessel functions, respectively. Previous studies have indicated that the aspect ratios based on digital cores are significantly higher than those derived from experimental data and theories (Sarout et al., 2017). The aspect ratios of stiff [0.01–1] and soft pores [ $<0.01$ ] are defined and used in many works (David & Zimmerman, 2012; Hudson, 1981; Zhang et al., 2021; Zhao et al., 2013), which are considered in this study. Moreover,  $K_d$  is the bulk modulus of the rock without microcracks, and  $K_{d,macro}$  is the bulk modulus of the rock containing only macroscopic stiff pores, which is obtained by adding the stiff pores to the rock mineral with the Mori-Tanaka theory (Mori & Tanaka, 1973), that is,

$$K_d = K_s / \left( 1 + \frac{\phi_{0,macro}}{1 - \phi_{0,macro}} P_{0,macro} \right), \quad (18)$$

where  $\phi_{0,macro}$  is the macroscopic stiff porosity, and  $P_{0,macro}$  is the corresponding polarization factor, which is related to the aspect ratio  $\alpha_{0,macro}$  of the pores and Poisson's ratio ( $\nu$ ) of the solid (Qi et al., 2021; Zhang et al., 2019) as

$$P_{0,macro} = \frac{(1 - \nu)}{6(1 - 2\nu)} \times \frac{4(1 + \nu) + 2\alpha_{0,macro}^2(7 - 2\nu) \cdot \times 3(1 + 4\nu) + 12\alpha_{0,macro}^2(2 - \nu)] g}{2\alpha_{0,macro}^2 + (1 - 4\alpha_{0,macro}^2) g + (\alpha_{0,macro}^2 - 1)(1 + \nu) g^2}, \quad (19)$$

respectively.  $P^{*2}$  and  $Q^{*2}$  are the geometrical factors of the microscopic pores or cracks (Berryman, 1980; Mavko et al., 2009).

Finally, Gurevich's squirt-flow model is used to obtain the wave responses of rock with fluid and complex structures. Gurevich et al. (2010) proposed a squirt flow model in which the compliant (soft) pores act as fluid flow channels to connect the stiff pores (see Carcione, 2022; Section 7.12). However, this model is not suitable for the multiscale pore structure investigated in this work, nor for the squirt flow effects of multiscale fractures. In recent years, the squirt flow model has been extended to a case with multiple crack aspect ratios (Sun & Gurevich, 2020; Wu et al., 2022). They study the case of multiple crack aspect ratios, and based on this idea, we consider two sets of squirt flow effects with large-scale cracks and small-scale cracks.

The bulk ( $K_{bf}$ ) and shear ( $G_{bf}$ ) dry-rock moduli, including squirt flow effects of the multiscale fractures, are obtained with (Sun & Gurevich, 2020)

$$\frac{1}{K_{bf}} = \frac{1}{K_d} + \frac{\phi_{c,micro}}{\left( \frac{1}{K_{dry}} \cdot \frac{1}{K_d} \right) + \left( \frac{1}{K_f^*} \cdot \frac{1}{K_s} \right)} + \frac{\phi_{c,macro}}{\left( \frac{1}{K_{eff}} \cdot \frac{1}{K_{d,macro}} \right) + \left( \frac{1}{K_f^*} \cdot \frac{1}{K_s} \right)}, \quad (14)$$

$$\frac{1}{G_{bf}} = \frac{1}{G_{dry}} \cdot \frac{4}{15} \left( \frac{1}{K_{dry}} \cdot \frac{1}{K_{bf}} \right), \quad (15)$$

$$K_f^* = \left( 1 - \frac{2J_1(\lambda)}{\lambda J_0(\lambda)} \right) K_f, \quad (16)$$

$$\lambda = \frac{1}{\alpha_{c,i}} \left( \frac{3i\omega\eta}{K_f} \right), \quad (17)$$

where  $\omega$  is the angular frequency,  $K_f$  is the fluid bulk modulus,  $\eta$  is the fluid viscosity,  $K_s$  is the bulk modulus of the grains,  $\phi_{c,macro}$  and  $\phi_{c,micro}$  are the porosities of the macrofractures and microcracks, respectively, and  $\alpha_{c,macro}/$

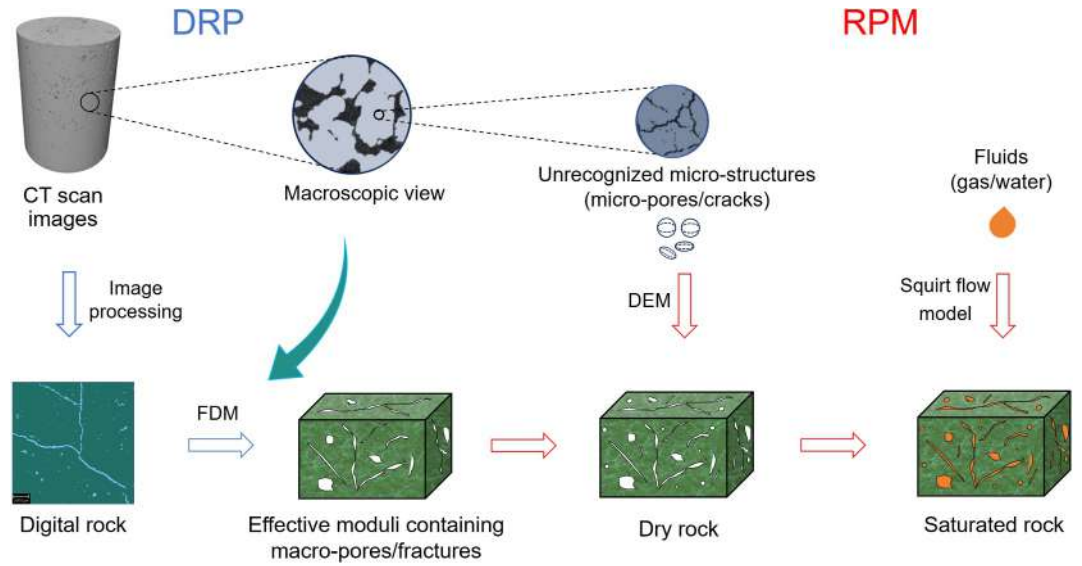


**Figure 22.** Flowchart of the reformulated rock physics model.

with,

$$v = (3K_S \cdot 2G_S) / (6K_S + 2G_S), \quad (20)$$

where  $G_S$  is the shear modulus of the grains, and

$$g = \begin{cases} \frac{\alpha_{0,\text{macro}}}{(1 - \alpha_{0,\text{macro}}^2)^{3/2}} \left( \arccos \alpha_{0,\text{macro}} \cdot \alpha_{0,\text{macro}} \sqrt{1 - \alpha_{0,\text{macro}}^2} \right) & (\alpha_{0,\text{macro}} < 1) \\ \frac{\alpha_{0,\text{macro}}}{(1 - \alpha_{0,\text{macro}}^2)^{3/2}} \left( \alpha_{0,\text{macro}} \sqrt{1 - \alpha_{0,\text{macro}}^2} \cdot \operatorname{arccosh} \alpha_{0,\text{macro}} \right) & (\alpha_{0,\text{macro}} > 1) \end{cases} \quad (21)$$

The P- and S-wave velocities and quality factors of the saturated rocks can be obtained as

$$V_S = \sqrt{\frac{G_{bf}}{\rho_{\text{sat}}}}, \quad (22)$$

$$V_P = \left[ \operatorname{Re} \left( \frac{1}{v_c} \right) \right]^{-1}, \quad (23)$$

$$Q_P = \frac{\operatorname{Re}(K_{\text{sat}} + 4G_{bf}/3)}{\operatorname{Im}(K_{\text{sat}} + 4G_{bf}/3)}, \quad (24)$$

respectively (Carcione, 2022), where the complex velocity is  $v_c = \sqrt{(K_{\text{sat}} + 4\mu_{\text{sat}}/3)/\rho}$ , and the rock density is  $\rho = \rho_s(1 - \phi) + \phi S_g \rho_g + \phi S_w \rho_w$ , where  $\rho_s$ ,  $\rho_g$ , and  $\rho_w$  are the densities of mineral, gas and water, respectively.  $\phi$  is the total porosity, which is the sum of macro- and micro-porosities, and  $K_{\text{sat}}$  is the bulk modulus of saturated rock obtained from the Gassmann equation (Gassmann, 1951).

## 5. Model and Data

The newly formulated RPM for carbonates with multi-scale pore structures is developed, which integrates numerical and theoretical rock physics to simulate seismic wave responses in rocks with different structures,

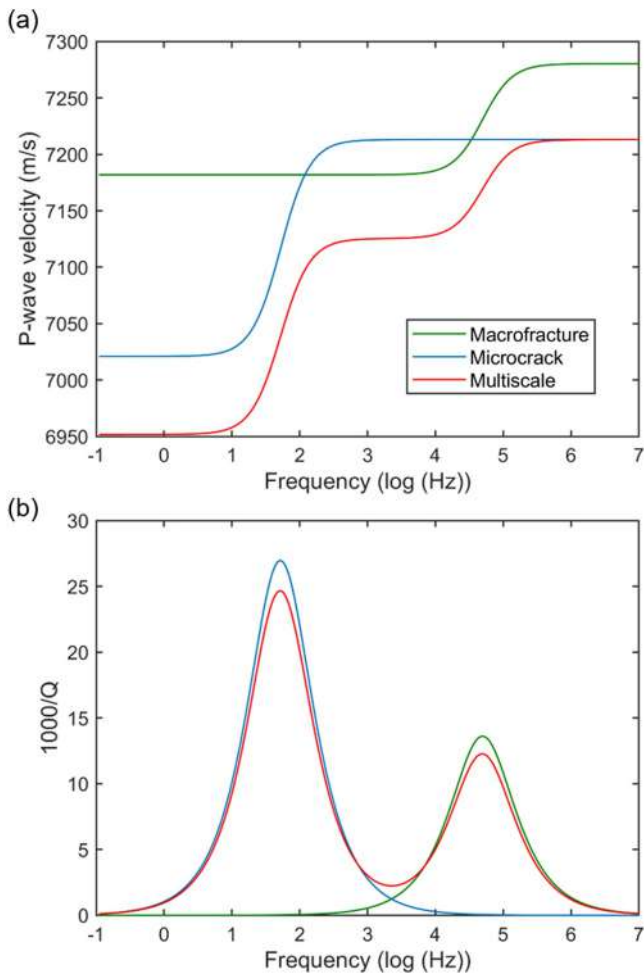


**Figure 23.** P-wave velocity (a) and attenuation (b) of sample DS\_A as a function of frequency for the multiscale structures.

interpret experimental data with multiple frequency bands under different pressures, and characterize multi-scale pore structures. The model results are verified with the experimental and logging data.

### 5.1. Model Results

The reformulated RPM can simulate the wave responses of carbonates with multiscale pore structures. The bulk modulus of water and gas is 2.24 and 0.017 GPa, the density is 1.002 g/cm<sup>3</sup> and 0.09 g/cm<sup>3</sup>, and the viscosity is  $7.8 \times 10^{-4}$  Pa s and  $9.6 \times 10^{-8}$  Pa s, respectively. We take sample DS\_A as an example and consider full water saturation. The volume fractions of the macroscopic pores are given in Table 3, and the other structural properties are:  $\phi_{0,micro} = 0.2\%$ ,  $\phi_{c,micro} = 0.001\%$ ,  $\alpha_{0,macro} = 1$ ,  $\alpha_{c,macro} = 0.0001$ ,  $\alpha_{0,micro} = 0.6$ , and  $\alpha_{c,micro} = 0.0001$ . Figure 23 shows the P-velocity dispersion and attenuation due to the multi-scale structure, as well as the responses caused by large fractures and small cracks alone (obtained from the Gurevich equations). The reformulated model can effectively compute the dispersion and attenuation of multi-scale structures, and two relaxation peaks are observed. Moreover, under the effects of multi-scale pores, the velocity is lower than that caused by the single structure, and the dispersion and attenuation are stronger.

Next, we model the effects of microcracks on wave dispersion and attenuation by adjusting the volume fraction and aspect ratio, as is shown in Figure 24. The parameters of the microcracks are given in the caption, the other properties are the same as in Figure 23. It is shown that P-wave velocity decreases and the attenuation increases as the content of microcracks increases, whereas the trends of velocity and attenuation are opposite as the aspect ratio increases. Moreover, the relaxation peaks shift to the lower frequencies as the aspect ratio increases.

### 5.2. Modeling Results and Data

The experimental multi-frequency data are used to verify the newly formulated RPM. Published studies based on CT tests at different pressures (1–20 MPa) suggested that the macro-pore space could be almost unchanged

with pressure variations (see Figure 6 in Saenger et al., 2016), thus, we assume that macro-pore properties from the scans are constant in the pressure range (1–25 MPa) of this study. For the measurements at different pressures, the simulations (Figures 25 and 26) can be effectively performed by varying the volume fractions of the microscopic pores and cracks in the model and keeping the aspect ratios constant; these properties of the multiscale structures are shown in Figures 28 and 29.

Figure 25 shows that the velocity of the P-wave in the water-saturated state varies with frequency, compared with experimental data under different pressures. The model agrees and interprets the multi-frequency data under different pressures for different structures and pressures. A dispersion of P-wave velocity due to elastic wave induced fluid flow can be observed. In addition, the frequency dependence shows different behaviors for different micro-pore structures and pressures, with the higher the pressure, the lower the dispersion (lower microcrack content).

It is clear that rocks with different pore types have different frequency sensitivities (Figure 25). To investigate the relationship between the frequency dependence and the pore structure, a further analysis is performed by closely examining the experimental data under 1 MPa effective pressure (Figure 26), which shows that the model agrees with the test results. The fractured samples (DS\_A, DS\_C, DS\_D) exhibit lower velocity, higher dispersion and stronger attenuation compared to the samples with pore cavity (DS\_E, DS\_F) and the fractured types (DS\_B). From the macroscopic view based on the rock images (Figures 3–5), there are many pores as well as fractures in the fractured-vuggy rock, resulting in a stronger squirt flow effect of the fluid between the pore structures. Based

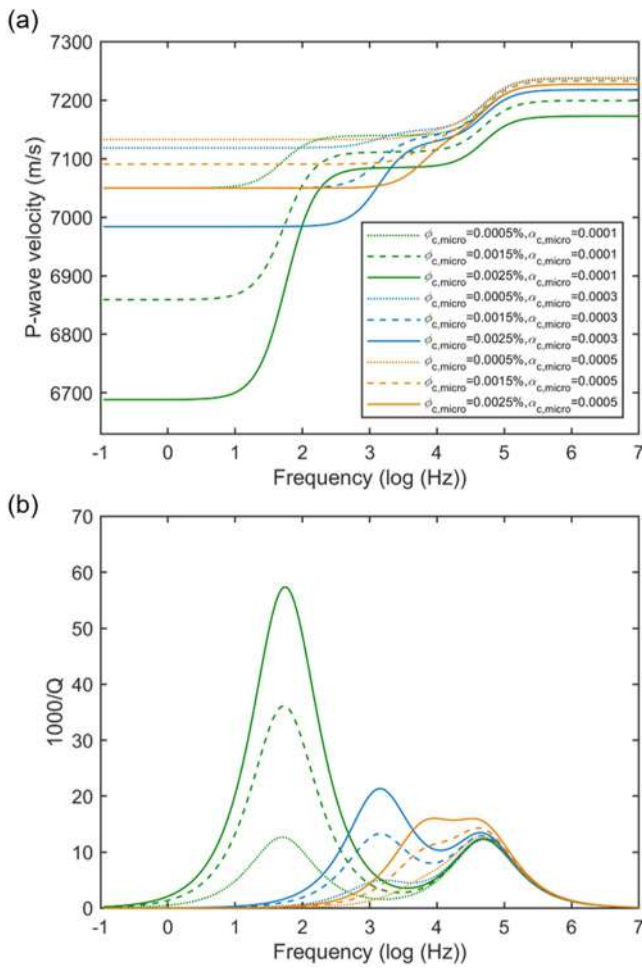


**Figure 24.** P-wave velocity (a) and attenuation (b) of sample DS\_A as a function of frequency with different microcracks properties.

on the characterized micro-pore structure (Figures 27 and 28), the underlying mechanisms can be further analyzed under the aspect of microporosity.

Figure 27 shows the multiscale pore structures characterized by the integration of the model and the multi-frequency data at water-saturated state. It can be seen that the content of microscopic pores and cracks changes at different pressures, indicating a decrease with increasing pressure, while the corresponding aspect ratio is constant with pressure. For different samples, the equivalent aspect ratios of the stiff pores may be the same, but the cracks have different aspect ratios. Then, we select the results at 1 MPa effective pressure to analyze the microporous properties of the samples with different pore types, as shown in Figure 28. It can be observed that the fractured-vuggy samples (DS\_A, DS\_C, DS\_D) have higher microcrack/porosity content than other types, as well as a corresponding squirt flow effect, which also explains the high-frequency dispersion and strong attenuation of rock from a microporous point of view. In addition, DS\_F has a lower microcrack porosity than DS\_E in the pore-cavity samples, which could explain the higher velocities of DS\_F (higher porosity) compared to DS\_E (lower porosity) in the experimental results (see Figure 15). Thus, this study provides an insight into the complex petrophysical behavior of tight rocks in terms of multiscale pore structure and reveals the wave response characteristics of rocks with different pore types.

We then simulate the elastic velocities ( $V_S$  and gas-saturated  $V_P$ ) based on the obtained pore structures (Figure 27) and compare them with the experimental data shown in Figure 29. Since there is no frequency dependence in  $V_S$  and  $V_P$  (gas) of the samples (Figures 9, 10, and 12), the ultrasonic measurements (which almost agree with the low-frequency results) at 25 MPa effective pressure are used to validate the model. The simulated results generally agree with the ultrasonic velocities, except that  $V_S$  of samples DS\_C and DS\_D and  $V_P$  of gas-saturated sample DS\_D are slightly higher. The results of the FD simulations (see Figure 21) are improved by including the RPM approach.

To further validate the model, we use borehole data from the working area as shown in Figure 30. The figure shows the wave velocities ( $V_P$ ,  $V_S$ ) for the reservoir section compared to the model results (10 kHz) for gas and water saturated cases at the sampling depths. The structural parameters were chosen at a pressure of 1 MPa. It can be observed that the wet samples DS\_A-DS\_E agree well with the formation data, while the gas-saturated samples (DS\_A, DS\_C, DS\_D) show a slightly lower  $V_P$ . In addition, DS\_F shows higher velocities than the sonic log data. This could be related to the fact that the reservoir rock is not fully saturated but partially saturated with a mixture of fluids (gas and water) and that fluid patches are present between the pore structures.

## 6. Conclusions

The pore structure and pore type of the six carbonate samples are analyzed by CT scans and thin sections of core samples, which show complex pore structures and different types. Based on the images, the rocks can be categorized into fractured, fractured-vuggy and pore-cavity.

The ultrasonic (1 MHz) and low frequency (1–100 Hz) experiments at different effective pressures (1–50 MPa or 1–25 MPa) and fluids (water/gas) are carried out to investigate the elastic properties. The velocities increase with pressure for both saturation states.  $V_P$  in the gas-saturated state and  $V_S$  are almost constant with frequency, while  $V_P$  in the wet state increases with frequency. The velocity dispersion is due to the fluid flow caused by the wave traveling through water-saturated porous rock.

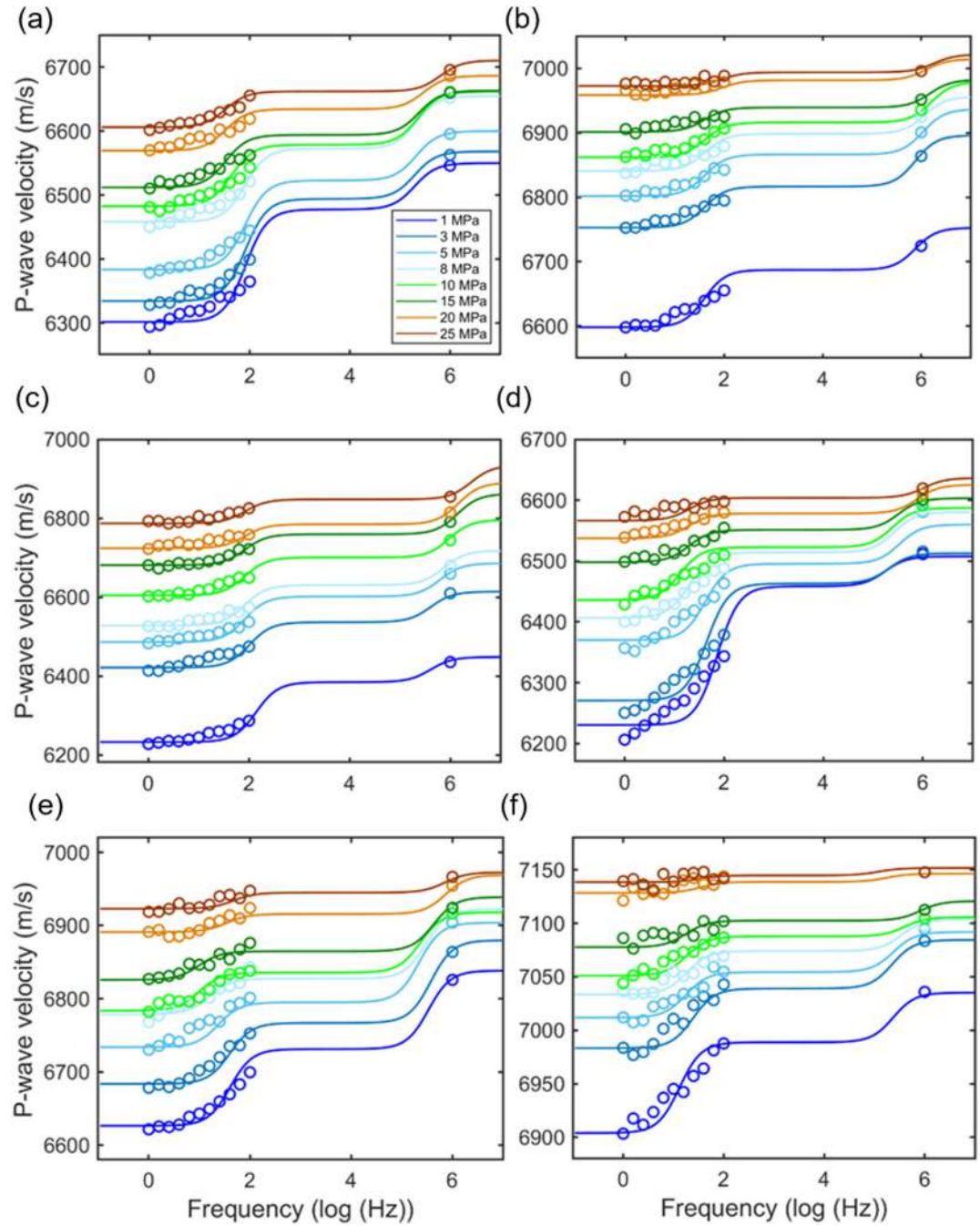


**Figure 25.** P-wave velocity as a function of frequency for the water-saturated samples compared with the multi-frequency-band experimental data at different effective pressures. (a), DS\_A; (b), DS\_B; (c), DS\_C; (d), DS\_D; (e), DS\_E; (f), DS\_F.

The rocks with pore cavities have higher velocities than the fractured-vuggy and fractured ones, with the fractured-vuggy type showing a greater velocity dispersion. In the saturated state with an effective pressure of 1 MPa, the dispersion of the fractured-vuggy samples DS\_A, DS\_C, and DS\_D is 4%, 3.3%, and 4.9%, respectively, while the dispersion of the fractured type (DS\_B) and pore-cavity (DS\_E and DS\_F) is lower.

The pore space can be divided into macropore and micropore structures, that is, those that can be detected by a CT scan and those that are not detected by the scan. Digital rock physics is used to calculate the effective moduli of

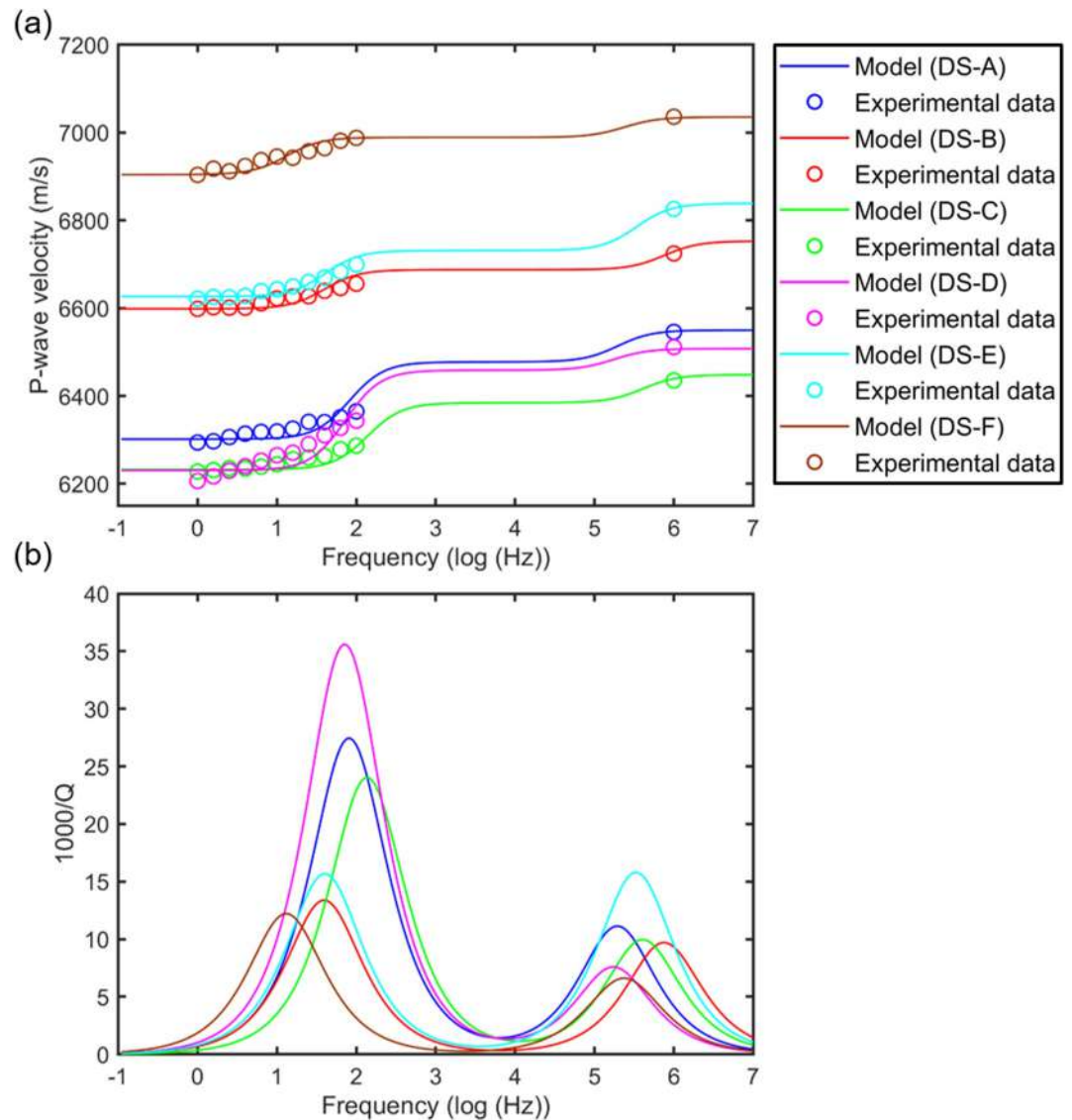


**Figure 26.** P-wave velocity dispersion and attenuation as a function of frequency for the water-saturated samples at 1 MPa effective pressure.

rocks with larger pores and fractures. Due to the limited scan resolution, the simulated elastic velocities are generally higher than the experimental results.

A newly formulated model is developed that can effectively simulate the wave responses and interpret multi-frequency data at different pressures by taking into account the different microstructural properties. By integrating digital and theoretical rock physics, the multiscale structures of the samples are characterized. The results show that the microcrack content of the fractured-vuggy type is higher than the other types, which is related to a strong anelasticity. In addition, the proposed model improves the estimated elastic properties of the FD simulations and illustrates the wave response mechanisms of rocks with different pore types.

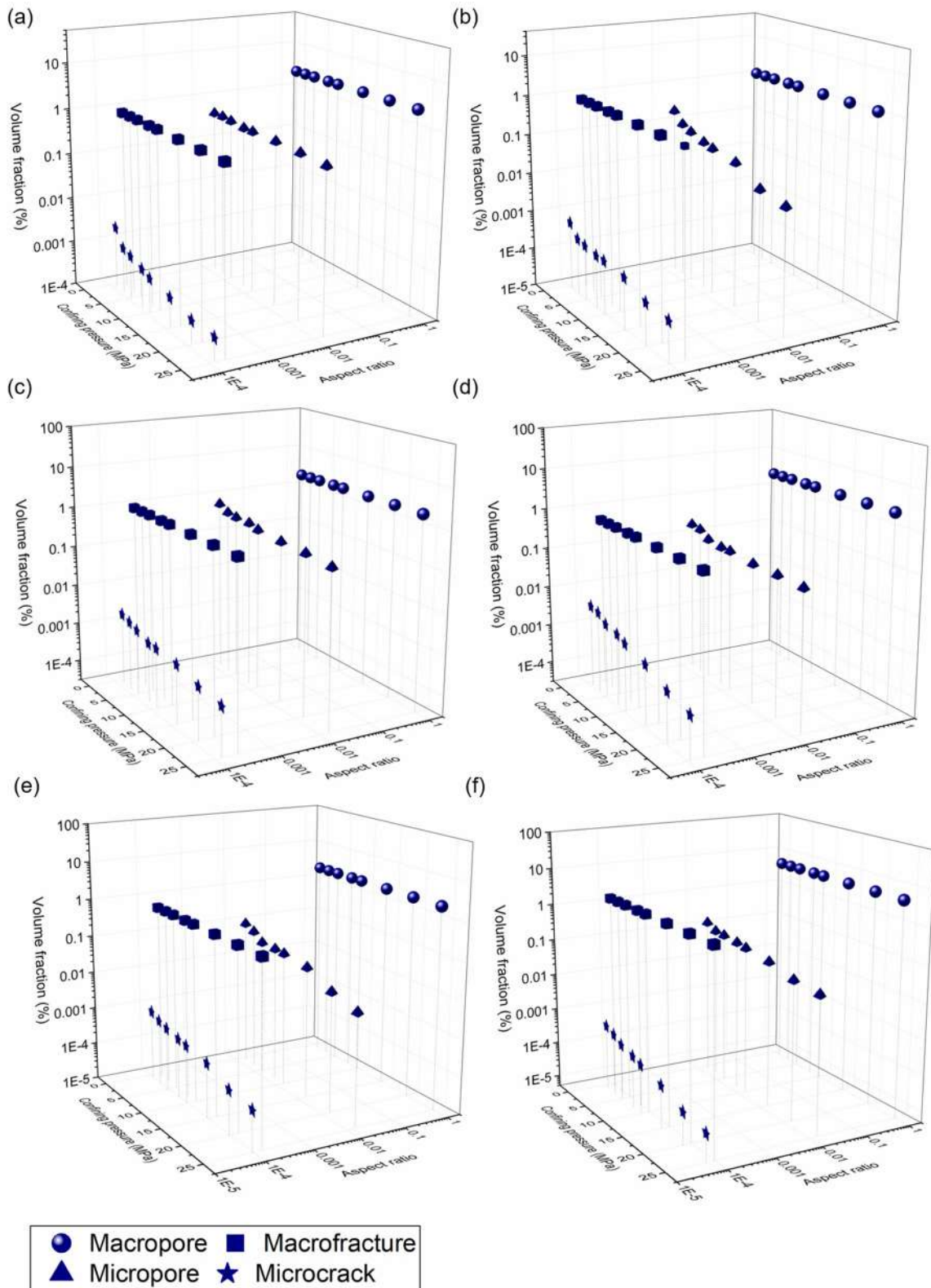


Figure 27. Multiscale pore structures of the samples at different pressures. (a), DS\_A; (b), DS\_B; (c), DS\_C; (d), DS\_D; (e), DS\_E; (f), DS\_F.

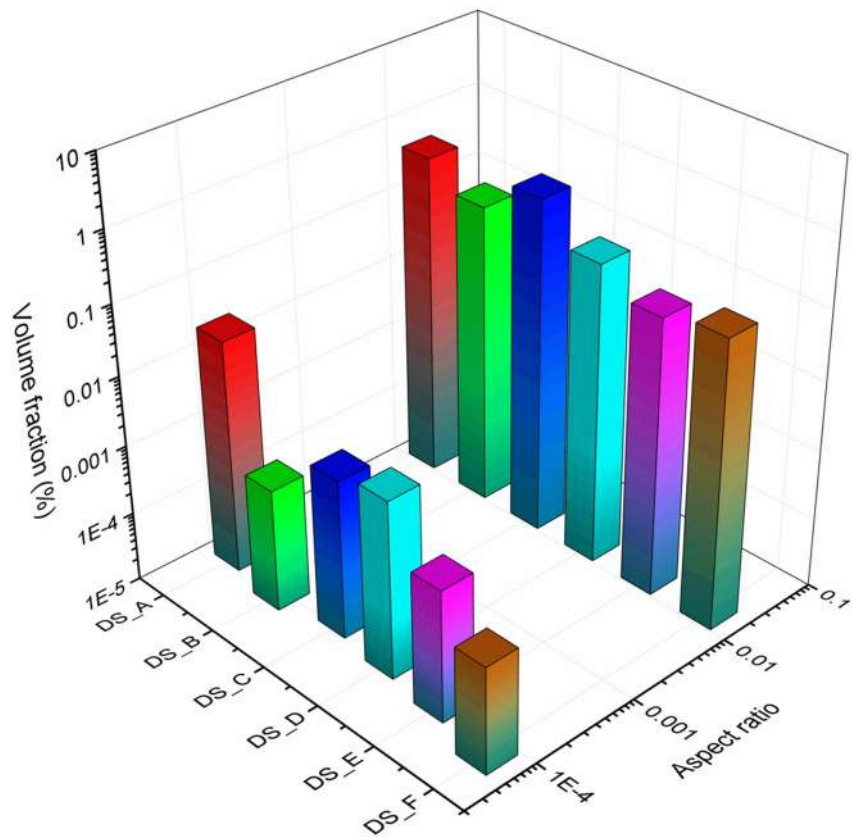


Figure 28. Micro-pore structures of the water-saturated samples at 1 MPa effective pressure.

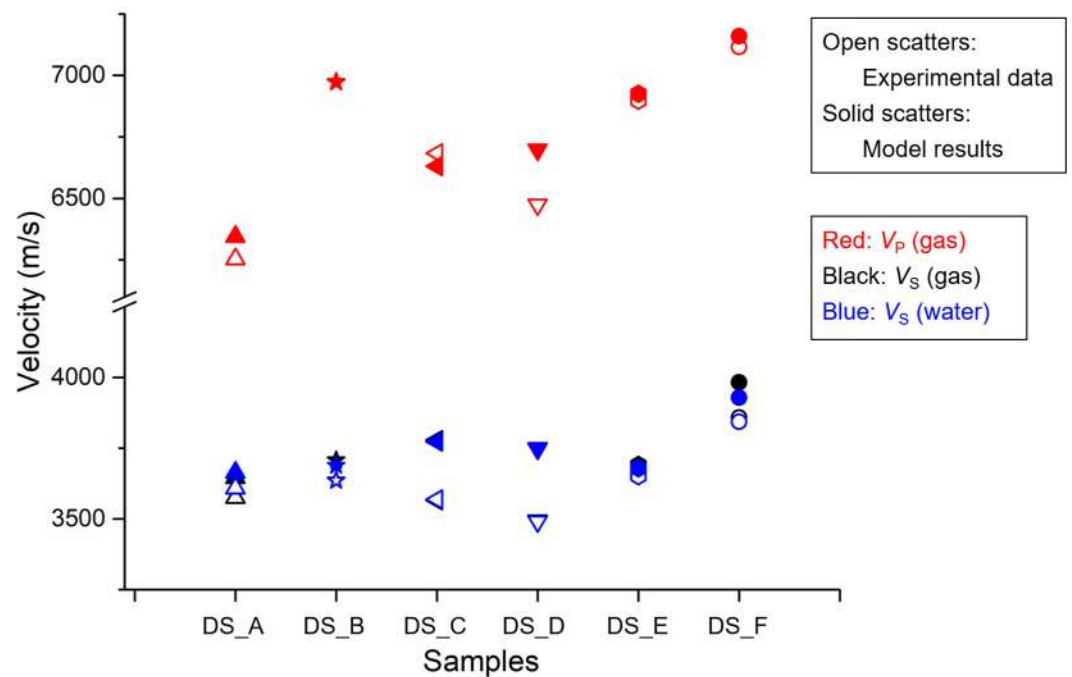
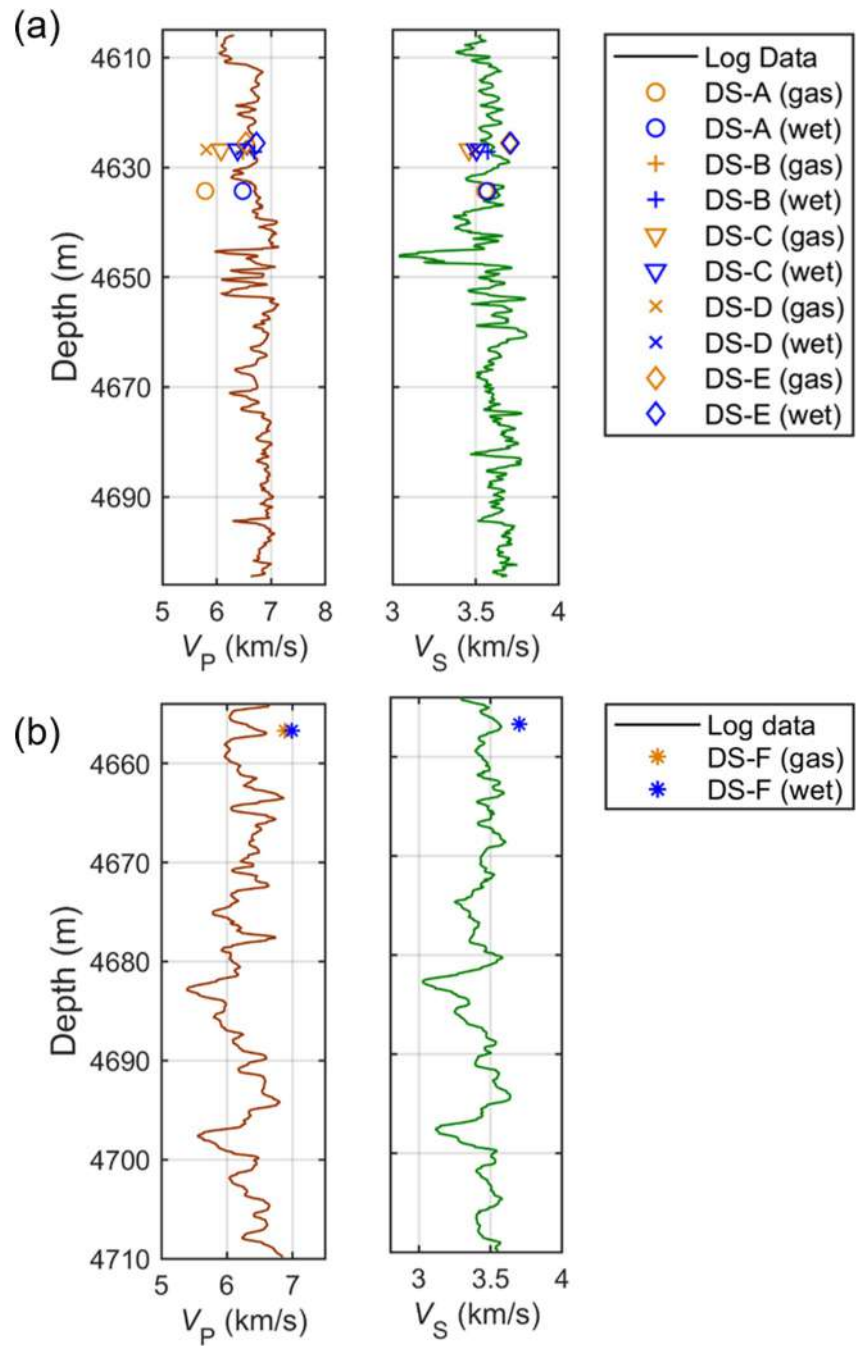


Figure 29. Model results with ultrasonic experimental data at 25 MPa effective pressure.



**Figure 30.** Model results with well A data (a. Samples DS\_A ~ DS\_E) and well B data (b. Sample DS\_F).

### Conflict of Interest

The authors declare no conflicts of interest relevant to this study.

### Data Availability Statement

The experimental measurement data and field data can be accessed at (Pang et al., 2025).

**Acknowledgments**

The work is supported by the Fundamental Research Funds for the Central Universities (B240201131), the National Natural Science Foundation of China (42174161) and the China Postdoctoral Science Foundation (2024M760744).

**References**

Agersborg, R., Johansen, T. A., & Jakobsen, M. (2009). Velocity variations in carbonate rocks due to dual porosity and wave-induced fluid flow. *Geophysical Prospecting*, 57(1), 81–98. <https://doi.org/10.1111/j.1365-2478.2008.00733.x>

Aliakbaridoust, E., & Rahimpour-Bonab, H. (2013). Effects of pore geometry and rock properties on water saturation of a carbonate reservoir. *Journal of Petroleum Science and Engineering*, 112, 296–309. <https://doi.org/10.1016/j.petrol.2013.11.018>

Al-Kharusi, A. S., & Blunt, M. J. (2007). Network extraction from sandstone and carbonate pore space images. *Journal of Petroleum Science and Engineering*, 56(4), 219–231. <https://doi.org/10.1016/j.petrol.2006.09.003>

Andrä, H., Combaret, N., Dvorkin, J., Glatt, E., Han, J., Kabel, M., et al. (2013a). Digital rock physics benchmarks—Part I: Imaging and segmentation. *Computers & Geosciences*, 50, 25–32. <https://doi.org/10.1016/j.cageo.2012.09.005>

Andrä, H., Combaret, N., Dvorkin, J., Glatt, E., Han, J., Kabel, M., et al. (2013b). Digital rock physics benchmarks—Part II: Computing effective properties. *Computers & Geosciences*, 50, 33–43. <https://doi.org/10.1016/j.cageo.2012.09.008>

Ba, J., Xu, W., Fu, L., Carcione, J., & Zhang, L. (2017). Rock anelasticity due to patchy-saturation and fabric heterogeneity: A double-double porosity model of wave propagation. *Journal of Geophysical Research: Solid Earth*, 122(3), 1949–1976. <https://doi.org/10.1002/2016JB013882>

Ba, J., Zhu, H., Zhang, L., & Carcione, J. M. (2023). Effect of multiscale cracks on seismic wave propagation in tight sandstones. *Journal of Geophysical Research: Solid Earth*, 128(10), e2023JB027474. <https://doi.org/10.1029/2023jb027474>

Bagrintseva, K. I., & Chilingar, G. V. (2007). Study of fractures and vugs in carbonate reservoirs. *Energy Sources, Part A: Recovery, Utilization, and Environmental Effects*, 30(1), 45–55. <https://doi.org/10.1080/15567030701568818>

Bailly, C., Fortin, J., Adelinet, M., & Hamon, Y. (2019). Upscaling of elastic properties in carbonates: A modeling approach based on a multiscale geophysical data set. *Journal of Geophysical Research: Solid Earth*, 124(12), 13021–13038. <https://doi.org/10.1029/2019jb018391>

Bazaikin, Y., Gurevich, B., Iglauer, S., Khachkova, T., Kolyukhin, D., Lebedev, M., et al. (2017). Effect of CT image size and resolution on the accuracy of rock property estimates. *Journal of Geophysical Research: Solid Earth*, 122(5), 3635–3647. <https://doi.org/10.1002/2016JB013575>

Berryman, J. G. (1980). Long-wavelength propagation in composite elastic media. *Journal of the Acoustical Society of America*, 68(6), 1809–1831.

Berryman, J. G. (1992). Single-scattering approximations for coefficients in Biot's equations of poroelasticity. *Acoustical Society of America Journal*, 91(2), 551–571. <https://doi.org/10.1121/1.402518>

Borgomano, J. V. M., Gallagher, A., Sun, C., & Fortin, J. (2020). An apparatus to measure elastic dispersion and attenuation using hydrostatic axial-stress oscillations under undrained conditions. *Review of Scientific Instruments*, 91(3), 034502. <https://doi.org/10.1063/1.5136329>

Borgomano, J. V. M., Pimienta, L., Fortin, J., & Guéguen, Y. (2017). Dispersion and attenuation measurements of the elastic moduli of a dual-porosity limestone. *Journal of Geophysical Research: Solid Earth*, 122(4), 2690–2711. <https://doi.org/10.1002/2016JB013816>

Borgomano, J. V. M., Pimienta, L. X., Fortin, J., & Guéguen, Y. (2019). Seismic dispersion and attenuation in fluid-saturated carbonate rocks: Effect of microstructure and pressure. *Journal of Geophysical Research: Solid Earth*, 124(12), 12498–12522. <https://doi.org/10.1029/2019JB018434>

Botha, P. W. S. K., & Sheppard, A. P. (2016). Mapping permeability in low-resolution micro-CT images: A multiscale statistical approach. *Water Resources Research*, 52(6), 4377–4398. <https://doi.org/10.1002/2015wr018454>

Carcione, J. M. (2022). *Wave fields in real media*. Elsevier.

Carcione, J. M., Gurevich, B., Santos, J. E., & Picotti, S. (2013). Angular and frequency-dependent wave velocity and attenuation in fractured porous media. *Pure and Applied Geophysics*, 170(11), 1673–1683. <https://doi.org/10.1007/s00024-012-0636-8>

Carcione, J. M., Morency, C., & Santos, J. E. (2010). Computational poroelasticity—A review. *Geophysics*, 75(5), 75A229–75A243. <https://doi.org/10.1190/1.3474602>

Carcione, J. M., Picotti, S., & Santos, J. E. (2012). Numerical experiments of fracture-induced velocity and attenuation anisotropy. *Geophysical Journal International*, 191(3), 1179–1191.

Chawshin, K., Gonzalez, A., Berg, C. F., Varagnolo, D., Heidari, Z., & Lopez, O. (2021). Classifying lithofacies from textural features in whole core CT-scan images. *SPE Reservoir Evaluation and Engineering*, 24(02), 341–357. <https://doi.org/10.2118/205354-pa>

David, E. C., & Zimmerman, R. W. (2012). Pore structure model for elastic wave velocities in fluid-saturated sandstones. *Journal of Geophysical Research*, 117(B7), B07210. <https://doi.org/10.1029/2012JB009195>

Delle Piane, C., Arena, A., Sarout, J., Esteban, L., & Cazes, E. (2015). Microcrack enhanced permeability in tight rocks: An experimental and microstructural study. *Tectonophysics*, 665, 149–156. <https://doi.org/10.1016/j.tecto.2015.10.001>

de Vries, E. T., Raouf, A., & van Genuchten, M. T. (2017). Multiscale modelling of dual-porosity porous media; a computational pore-scale study for flow and solute transport. *Advances in Water Resources*, 105, 82–95. <https://doi.org/10.1016/j.advwatres.2017.04.013>

Dubiel, S., Zubrzycki, A., Rybicki, C., & Maruta, M. (2012). Application of DST interpretation results by log–log method in the pore space type estimation for the Upper Jurassic carbonate reservoir rocks of the Carpathian Foredeep basement. *Archives of Mining Sciences*, 57(2), 413–424. <https://doi.org/10.2478/v10267-012-0027-0>

Durrani, M. Z. A., Rahman, S. A., Talib, M., Subhani, G., & Sarosh, B. (2023). Rock physics modelling-based characterization of deep and tight mixed sedimentary (clastic and carbonate) reservoirs: A case study from North Potwar Basin of Pakistan. *Geophysical Prospecting*, 71(2), 263–278. <https://doi.org/10.1111/1365-2478.13288>

Dvorkin, J., Derzhi, N., Diaz, E., & Fang, Q. (2011). Relevance of computational rock physics. *Geophysics*, 76(5), E141–E153. <https://doi.org/10.1190/geo2010-0352.1>

El-Bagoury, M. (2024). Petrophysical and petrographical delineation for carbonate reservoir rocks in north Western Desert, Egypt. *Carbonates and Evaporites*, 39(3), 84. <https://doi.org/10.1007/s13146-024-00996-9>

Garboczi, E. J., & Day, A. R. (1995). An algorithm for computing the effective linear elastic properties of heterogeneous materials: Three-dimensional results for composites with equal phase Poisson ratio. *Journal of the Mechanics and Physics of Solids*, 43(9), 1349–1362. [https://doi.org/10.1016/0022-5096\(95\)00050-s](https://doi.org/10.1016/0022-5096(95)00050-s)

Gassmann, F. (1951). Elasticity of porous media. *Vierteljahrsschrder Naturforschenden Gessellschaft*, 96, 1–23.

Gonzalez, A., Heidari, Z., & Lopez, O. (2022). Integration of 3D volumetric computed tomography scan image data with conventional well logs for detection of petrophysical rock classes. *SPE Reservoir Evaluation and Engineering*, 25(02), 146–162. <https://doi.org/10.2118/208605-pa>

Guo, J., Chen, X., Zhao, J., & Xiao, Z. (2024). Effects of background elastic and permeability anisotropy on dynamic seismic signatures of a fluid-saturated porous rock with aligned fractures. *Geophysics*, 89(6), MR335–MR354. <https://doi.org/10.1190/geo2024-0377.1>

Guo, J., & Fu, B. (2024). Effective elastic properties of fractured rocks considering fracture interactions. *Geophysical Prospecting*, 73(1), 330–344. <https://doi.org/10.1111/1365-2478.13632>

- Guo, J., Gurevich, B., & Chen, X. (2022). Dynamic SV wave signatures of fluid saturated porous rocks containing intersecting fractures. *Journal of Geophysical Research: Solid Earth*, 127(8), e2022JB024745. <https://doi.org/10.1029/2022jb024745>
- Gurevich, B., Brajanovski, M., Galvin, R. J., Müller, T. M., & Toms-Stewart, J. (2009). P-wave dispersion and attenuation in fractured and porous reservoirs—poroelasticity approach. *Geophysical Prospecting*, 57(2), 225–237. <https://doi.org/10.1111/j.1365-2478.2009.00785.x>
- Gurevich, B., Makarynska, D., de Paula, O. B., & Pervukhina, M. (2010). A simple model for squirt-flow dispersion and attenuation in fluid-saturated granular rocks. *Geophysics*, 75(6), N109–N120. <https://doi.org/10.1190/1.3509782>
- He, J., Li, M., Zhou, K. Z., Yang, Y., Xie, B., Li, N., et al. (2020). Effects of vugs on resistivity of vuggy carbonate reservoirs. *Petroleum Exploration and Development*, 47(3), 527–535. [https://doi.org/10.1016/s1876-3804\(20\)60070-2](https://doi.org/10.1016/s1876-3804(20)60070-2)
- Hudson, J. A. (1981). Wave speeds and attenuation of elastic waves in material containing cracks. *Geophysical Journal International*, 64(1), 133–150. <https://doi.org/10.1111/j.1365-246x.1981.tb02662.x>
- Jin, X., Dou, Q., Hou, J., Huang, Q., Sun, Y., Jiang, Y., et al. (2017). Rock-physics-model-based pore type characterization and its implication for porosity and permeability qualification in a deeply-buried carbonate reservoir, Changxing formation, Lower Permian, Sichuan Basin, China. *Journal of Petroleum Science and Engineering*, 153, 223–233. <https://doi.org/10.1016/j.petrol.2017.02.003>
- Kadryov, R., Nurgaliev, D., Saenger, E. H., Balcewicz, M., Minebaev, R., Statsenko, E., et al. (2022). Digital rock physics: Defining the reservoir properties on drill cuttings. *Journal of Petroleum Science and Engineering*, 210, 110063. <https://doi.org/10.1016/j.petrol.2021.110063>
- Karimpouli, S., Kadryov, R., Siegart, M., & Saenger, E. H. (2023). Applicability of 2D algorithms in digital rocks physics for 3D characterization: An example of a machine learning based super resolution image generation. *Acta Geophysica*, 1–14. <https://doi.org/10.1007/s11600-023-01149-7>
- Keehm, Y. (2003). *Computational rock physics: Transport properties in porous media and applications*. PhD Thesis[D]. Stanford University.
- Lai, J., & Wang, G. (2015). Fractal analysis of tight gas sandstones using high-pressure mercury intrusion techniques. *Journal of Natural Gas Science and Engineering*, 24, 185–196. <https://doi.org/10.1016/j.jngse.2015.03.027>
- Lan, X., Lu, X., Zhu, Y., & Yu, H. (2015). The geometry and origin of strike-slip faults cutting the Tazhong low rise megaanticline (central uplift, Tarim Basin, China) and their control on hydrocarbon distribution in carbonate reservoirs. *Journal of Natural Gas Science and Engineering*, 22, 633–645. <https://doi.org/10.1016/j.jngse.2014.12.030>
- Latif, F. D. E., & Feranie, S. (2014). Three-dimensional visualization and characterization of cracks in geothermal reservoir rock using image analysis of reconstructed  $\mu$ CT images: A preliminary study. In *AIP Conference Proceedings* (Vol. 1589, pp. 120–123). American Institute of Physics. <https://doi.org/10.1063/1.4868764>
- Li, M., Zhao, Y., & Zhang, P. (2016). Attenuator design method for dedicated whole-core CT. *Optics Express*, 24(20), 22749–22765. <https://doi.org/10.1364/oe.24.022749>
- Li, W., Mu, L., Zhao, L., Li, J., Wang, S., Fan, Z., et al. (2020). Pore-throat structure characteristics and its impact on the porosity and permeability relationship of Carboniferous carbonate reservoirs in eastern edge of Pre-Caspian Basin. *Petroleum Exploration and Development*, 47(5), 1027–1041. [https://doi.org/10.1016/s1876-3804\(20\)60114-8](https://doi.org/10.1016/s1876-3804(20)60114-8)
- Li, X., Li, C., Li, B., Liu, X., & Yuan, C. (2020b). Response laws of rock electrical property and saturation evaluation method of tight sandstone. *Petroleum Exploration and Development*, 47(1), 214–224. [https://doi.org/10.1016/s1876-3804\(20\)60020-9](https://doi.org/10.1016/s1876-3804(20)60020-9)
- Li, Z., Ni, G., Wang, Y., Jiang, H., Wen, Y., Dou, H., & Jing, M. (2022). Semi-homogeneous model of coal based on 3D reconstruction of CT images and its seepage-deformation characteristics. *Energy*, 259, 125044. <https://doi.org/10.1016/j.energy.2022.125044>
- Liang, J., Wen, H., Li, X., Qiao, Z., She, M., Zhong, Y., & Zhang, H. (2023). Research progress of burial dissolution and modification of carbonate reservoirs and fluid-rock simulation experiments. *Earth Science*, 48(2), 814–834. <https://doi.org/10.3799/dqkx.2023.031>
- Lissa, S., Ruf, M., Steeb, H., & Quintal, B. (2021). Digital rock physics applied to squirt flow. *Geophysics*, 86(4), MR235–MR245. <https://doi.org/10.1190/geo2020-0731.1>
- Lubis, L. A., & Harith, Z. Z. T. (2014). Pore type classification on carbonate reservoir in offshore Sarawak using rock physics model and rock digital images. *IOP Conference Series: Earth and Environmental Science*, 19(1), 012003. <https://doi.org/10.1088/1755-1315/19/1/012003>
- Lv, J., Cheng, Z., Xue, K., Liu, Y., & Mu, H. (2020). Pore-scale morphology and wettability characteristics of xenon hydrate in sand matrix—Laboratory visualization with micro-CT. *Marine and Petroleum Geology*, 120, 104525. <https://doi.org/10.1016/j.marpetgeo.2020.104525>
- Madonna, C., Quintal, B., Frehner, M., Almqvist, B. S., Tisato, N., Pistone, M., et al. (2013). Synchrotron-based X-ray tomographic microscopy for rock physics investigations. *Geophysics*, 78(1), D53–D64. <https://doi.org/10.1190/geo2012-0113.1>
- Malki, M. L., Saberi, M. R., Kolawole, O., Rasouli, V., Sennaoui, B., & Ozotta, O. (2023). Underlying mechanisms and controlling factors of carbonate reservoir characterization from rock physics perspective: A comprehensive review. *Geoenergy Science and Engineering*, 226, 211793. <https://doi.org/10.1016/j.jgeoen.2023.211793>
- Mavko, G., Mukerji, T., & Dvorkin, J. (2009). *The rock physics handbook: Tools for seismic analysis of porous media*. Cambridge University Press.
- Mena-Negrete, J., Valdiviezo-Mijangos, O. C., Nicolás-López, R., & Coconi-Morales, E. (2022). Characterization of elastic moduli with anisotropic rock physics templates considering mineralogy, fluid, porosity, and pore-structure: A case study in Volve field, North Sea. *Journal of Applied Geophysics*, 206, 104815. <https://doi.org/10.1016/j.jappgeo.2022.104815>
- Misaghi, A., Negahban, S., Landrø, M., & Javaherian, A. (2010). A comparison of rock physics models for fluid substitution in carbonate rocks. *Exploration Geophysics*, 41(2), 146–154. <https://doi.org/10.1071/eg09035>
- Mollajan, A., & Memarian, H. (2016). Rock physics-based carbonate pore type identification using Parzen classifier. *Journal of Petroleum Science and Engineering*, 145, 205–212. <https://doi.org/10.1016/j.petrol.2016.03.021>
- Mori, T., & Tanaka, K. (1973). Average stress in matrix and average elastic energy of materials with misfitting inclusions. *Acta Metallurgica*, 21(5), 571–574. [https://doi.org/10.1016/0001-6160\(73\)90064-3](https://doi.org/10.1016/0001-6160(73)90064-3)
- Okabe, H., & Blunt, M. J. (2004). Prediction of permeability for porous media reconstructed using multiple-point statistics. *Physical Review E - Statistical, Nonlinear and Soft Matter Physics*, 70(2), 066135. <https://doi.org/10.1103/physreve.70.066135>
- Okabe, H., & Blunt, M. J. (2007). Pore space reconstruction of vuggy carbonates using microtomography and multiple-point statistics. *Water Resources Research*, 43(12). <https://doi.org/10.1029/2006WR005680>
- Pang, M., Ba, J., Carcione, J., Picotti, S., Zhou, J., & Jiang, R. (2019). Estimation of porosity and fluid saturation in carbonates from rock-physics templates based on seismic Q. *Geophysics*, 84(6), M25–M36. <https://doi.org/10.1190/geo2019-0031.1>
- Pang, M., Ba, J., Carcione, J. M., Balcewicz, M., Siegart, M., Tang, G., & Saenger, E. H. (2025). Structural and elastic properties of carbonate rocks with different pore types based on digital and theoretical rock physics. *Mendeley Data*, V2. <https://doi.org/10.17632/b6n9m3dk3r.2>
- Pang, M., Ba, J., Carcione, J. M., Balcewicz, M., Yue, W., & Saenger, E. H. (2022). Acoustic and electrical properties of tight rocks: A comparative study between experiment and theory. *Surveys in Geophysics*, 43(6), 1–31. <https://doi.org/10.1007/s10712-022-09730-3>
- Pang, M., Ba, J., Carcione, J. M., Yang, Z., & Saenger, E. (2024a). Petro-elastic model of the multiple pore-crack structure of carbonate rocks based on digital cores. *Acta Geophysica*. <https://doi.org/10.1007/s11600-024-01416-1>

- Pang, M., Balcewicz, M., Ba, J., Carcione, J. M., Siegert, M., & Saenger, E. (2024b). Acoustical-electrical models of tight rocks based on digital rock physics and double-porosity theory. *Geoenergy Sci Eng*, 235, 212634. <https://doi.org/10.1016/j.geoen.2024.212634>
- Peng, S., Marone, F., & Dultz, S. (2014). Resolution effect in X-ray microcomputed tomography imaging and small pore's contribution to permeability for a Berea sandstone. *Journal of Hydrology*, 510, 403–411. <https://doi.org/10.1016/j.jhydrol.2013.12.028>
- Phukan, R., Saha, R., & Mazumdar, P. (2024). Adsorption behavior of surfactants on sandstone reservoir rocks with carbonate cements and its influence on wettability alteration. *Journal of Surfactants and Detergents*, 27(3), 393–408. <https://doi.org/10.1002/jsde.12727>
- Qi, C., Liu, Y., Dong, F., Liu, X., Yang, X., Shen, Y., & Huang, H. (2020). Study on heterogeneity of pore throats at different scales and its influence on seepage capacity in different types of tight carbonate reservoirs. *Geofluids*, 1, 6657660.
- Qi, H., Ba, J., & Müller, T. M. (2021). Temperature effect on the velocity-porosity relationship in rocks. *Journal of Geophysical Research: Solid Earth*, 126(1), e2019JB019317. <https://doi.org/10.1029/2019JB019317>
- Qin, X., Xia, Y., Wu, J., Sun, C., Zeng, J., Xu, K., & Cai, J. (2022). Influence of pore morphology on permeability through digital rock modeling: New insights from the Euler number and shape factor. *Energy & Fuels*, 36(14), 7519–7530. <https://doi.org/10.1021/acs.energyfuels.2c01359>
- Rosid, M. S., Wahyuni, S. D., & Haidar, M. W. (2017). Carbonate reservoir characterization with pore type inversion using differential effective medium (DEM) model at “X” field, East Java. In *AIP Conference Proceedings* (Vol. 1862, p. 030179). AIP Publishing. <https://doi.org/10.1063/1.4991283>
- Saenger, E. H., & Bohlen, T. (2004). Finite-difference modeling of viscoelastic and anisotropic wave propagation using the rotated staggered grid. *Geophysics*, 69(2), 583–591. <https://doi.org/10.1190/1.1707078>
- Saenger, E. H., Gold, N., & Shapiro, S. A. (2000). Modeling the propagation of elastic waves using a modified finite-difference grid. *Wave Motion*, 31(1), 77–92. [https://doi.org/10.1016/s0165-2125\(99\)00023-2](https://doi.org/10.1016/s0165-2125(99)00023-2)
- Saenger, E. H., Lebedev, M., Uribe, D., Osorno, M., Vialle, S., Duda, M., et al. (2016). Analysis of high-resolution X-ray computed tomography images of Bentheim sandstone under elevated confining pressures. *Geophysical Prospecting*, 64(4), 848–859. <https://doi.org/10.1111/1365-2478.12400>
- Saenger, E. H., Shapiro, S. A., & Keehm, Y. (2005). Seismic effects of viscous Biot-coupling: Finite difference simulations on micro-scale. *Geophysical Research Letters*, 32(14), 337–349. <https://doi.org/10.1029/2005gl023222>
- Saenger, E. H., Vialle, S., Lebedev, M., Uribe, D., Osorno, M., Duda, M., & Steeb, H. (2016). Digital carbonate rock physics. *Solid Earth*, 7(4), 1185–1197. <https://doi.org/10.5194/se-7-1185-2016>
- Sakhaee-Pour, A., & Bryant, S. L. (2014). Effect of pore structure on the producibility of tight-gas sandstones. *AAPG Bulletin*, 98(4), 663–694. <https://doi.org/10.1306/08011312078>
- Sarout, J., Cazes, E., Delle Piane, C., Arena, A., & Esteban, L. (2017). Stressdependent permeability and wave dispersion in tight cracked rocks: Experimental validation of simple effective medium models. *Journal of Geophysical Research: Solid Earth*, 122(8), 6180–6201. <https://doi.org/10.1002/2017JB014147>
- Saxena, N., Hofmann, R., Hows, A., Saenger, E. H., Duranti, L., Stefani, J., et al. (2019). Rock compressibility from microcomputed tomography images: Controls on digital rock simulations. *Geophysics*, 84(4), WA127–WA139. <https://doi.org/10.1190/geo2018-0499.1>
- She, M., Shou, J., Shen, A., Pan, L., Hu, A., & Hu, Y. (2016). Experimental simulation of dissolution law and porosity evolution of carbonate rock. *Petroleum Exploration and Development*, 43(4), 616–625. [https://doi.org/10.1016/s1876-3804\(16\)30072-6](https://doi.org/10.1016/s1876-3804(16)30072-6)
- Siegert, M., Gurriss, M., Lebedev, M., & Saenger, E. H. (2022). Numerical modeling of the permeability in Bentheim sandstone under confining pressure. 88, 1–62. <https://doi.org/10.1190/geo2021-07181>
- Singh, A., Rabbani, A., Regenauer-Lieb, K., Armstrong, R. T., & Mostaghimi, P. (2021). Computer vision and unsupervised machine learning for pore-scale structural analysis of fractured porous media. *Advances in Water Resources*, 147, 103801. <https://doi.org/10.1016/j.advwatres.2020.103801>
- Spencer, J. W. (1981). Stress relaxations at low frequencies in fluid-saturated rocks: Attenuation and modulus dispersion. *Journal of Geophysical Research*, 86(B3), 1803–1812. <https://doi.org/10.1029/JB086iB03p01803>
- Sun, C., Fortin, J., Borgomano, J. V., Wang, S., Tang, G., Bultreys, T., & Cnudde, V. (2022). Influence of fluid distribution on seismic dispersion and attenuation in partially saturated limestone. *Journal of Geophysical Research: Solid Earth*, 127(5), e2021JB023867. <https://doi.org/10.1029/2021jb023867>
- Sun, H., Duan, L., Liu, L., Fan, W., Fan, D., Yao, J., et al. (2019). The influence of micro-fractures on the flow in tight oil reservoirs based on pore-network models. *Energies*, 12(21), 4104. <https://doi.org/10.3390/en12214104>
- Sun, Y., & Gurevich, B. (2020). Modeling the effect of pressure on the moduli dispersion in fluid-saturated rocks. *Journal of Geophysical Research: Solid Earth*, 125(12), e2019JB019297. <https://doi.org/10.1029/2019jb019297>
- Tahmasebi, P., & Kamrava, S. (2018). Rapid multiscale modeling of flow in porous media. *Physical Review E - Statistical Physics, Plasmas, Fluids, and Related Interdisciplinary Topics*, 98(5), 052901. <https://doi.org/10.1103/PhysRevE.98.052901>
- Tan, M., Su, M., Liu, W., Song, X., & Wang, S. (2021). Digital core construction of fractured carbonate rocks and pore-scale analysis of acoustic properties. *Journal of Petroleum Science and Engineering*, 196, 107771. <https://doi.org/10.1016/j.petrol.2020.107771>
- Wang, S., Tan, M., Wang, X., & Zhang, L. (2022). Microscopic response mechanism of electrical properties and saturation model establishment in fractured carbonate rocks. *Journal of Petroleum Science and Engineering*, 208, 109429. <https://doi.org/10.1016/j.petrol.2021.109429>
- Wu, C. F., Ba, J., Carcione, J. M., Müller, T. M., & Zhang, L. (2022). A patchy-saturated rock physics model for tight sandstone based on microscopic pore structures. *Applied Geophysics*, 19(2), 147–160. <https://doi.org/10.1007/s11770-022-0938-2>
- Wu, H., Li, F., Liu, J., Chen, J., Lv, X., & Hu, W. (2016). An experimental study on low-velocity nonlinear flow in vuggy carbonate reservoirs. *Geosystem Engineering*, 19(4), 151–157. <https://doi.org/10.1080/12269328.2016.1156586>
- Wu, J., Fan, T., Gomez-Rivas, E., Gao, Z., Yao, S., Li, W., et al. (2019). Impact of pore structure and fractal characteristics on the sealing capacity of Ordovician carbonate cap rock in the Tarim Basin, China. *Marine and Petroleum Geology*, 102, 557–579. <https://doi.org/10.1016/j.marpetgeo.2019.01.014>
- Yu, H., Zhang, Y., Lebedev, M., Wang, Z., Li, X., Squelch, A., et al. (2019). X-ray micro-computed tomography and ultrasonic velocity analysis of fractured shale as a function of effective stress. *Marine and Petroleum Geology*, 110, 472–482. <https://doi.org/10.1016/j.marpetgeo.2019.07.015>
- Yue, H., Liu, H., Hua, H., Han, J., & Wang, F. (2024). Comprehensive pore structure characterization and permeability prediction of carbonate reservoirs using high-pressure mercury intrusion and X-ray CT. *Carbonates and Evaporites*, 39(2), 18. <https://doi.org/10.1007/s13146-024-00923-y>
- Zhang, L., Ba, J., & Carcione, J. M. (2021). Wave propagation in infinituple-porosity media. *Journal of Geophysical Research: Solid Earth*, 126(4), e2020JB021266. <https://doi.org/10.1029/2020jb021266>
- Zhang, L., Ba, J., Carcione, J. M., & Wu, C. (2022). Seismic wave propagation in partially saturated rocks with a fractal distribution of fluid-patch size. *Journal of Geophysical Research: Solid Earth*, 127(2), e2021JB023809. <https://doi.org/10.1029/2021jb023809>

- Zhang, L., Ba, J., Fu, L., Carcione, J. M., & Cao, C. (2019). Estimation of pore microstructure by using the static and dynamic moduli. *International Journal of Rock Mechanics and Mining Sciences*, *113*, 24–30. <https://doi.org/10.1016/j.ijrmms.2018.11.005>
- Zhao, L., Nasser, M., & Han, D. (2013). Quantitative geophysical pore-type characterization and its geological implication in carbonate reservoirs. *Geophysical Prospecting*, *61*(4), 827–841. <https://doi.org/10.1111/1365-2478.12043>
- Zhao, L., Wang, S. Q., Zhao, W. Q., Luo, M., Wang, C. G., Cao, H. L., & He, L. (2016). Combination and distribution of reservoir space in complex carbonate rocks. *Petroleum Science*, *13*(3), 450–462. <https://doi.org/10.1007/s12182-016-0117-2>
- Zhu, B., Meng, J., Pan, R., Song, C., Zhu, Z., Jin, J., et al. (2023a). Multi-scale characterization of organic matter pore space in deep marine shale combined with mathematical morphology. *Geoenergy Science and Engineering*, *223*, 211539. <https://doi.org/10.1016/j.geoen.2023.211539>
- Zhu, W., Zhao, L., Yang, Z., Cao, H., Wang, Y., Chen, W., & Shan, R. (2023b). Stress relaxing simulation on digital rock: Characterize attenuation due to wave-induced fluid flow and scattering. *Journal of Geophysical Research: Solid Earth*, *128*(2), e2022JB024850. <https://doi.org/10.1029/2022jb024850>
- Zou, C., Zhao, L., Hong, F., Wang, Y., Chen, Y., & Geng, J. (2023). A comparison of machine learning methods to predict porosity in carbonate reservoirs from seismic-derived elastic properties. *Geophysics*, *88*(2), B101–B120. <https://doi.org/10.1190/geo2021-0342.1>